Dalton Transactions

ROYAL SOCIETY OF CHEMISTRY

PAPER

View Article Online
View Journal | View Issue

Check for updates

Cite this: *Dalton Trans.*, 2022, **51**, 2674

Tunable TiO_2–BN–Pd nanofibers by combining electrospinning and atomic layer deposition to enhance photodegradation of acetaminophen†

Syreina Sayegh,[a,b] Fida Tanos,[a,b] Amr Nada,[a,c] Geoffroy Lesage,[a] François Zaviska,[a] Eddy Petit,[a] Vincent Rouessac,[a] Igor Iatsunskyi,[d] Emerson Coy,[d] Roman Viter,[e,f] Daina Damberga,[e] Matthieu Weber,[g] Antonio Razzouk,[b] Juliette Stephan[b] and Mikhael Bechelany*[a]

The demand for fresh and clean water sources is increasing globally, and there is a need to develop novel routes to eliminate micropollutants and other harmful species from water. Photocatalysis is a promising alternative green technology that has shown great performance in the degradation of persistent pollutants. Titanium dioxide is the most used catalyst owing to its attractive physico-chemical properties, but this semiconductor presents limitations in the photocatalysis process due to the high band gap and the fast recombination of the photogenerated carriers. Herein, a novel photocatalyst has been developed, based on titanium dioxide nanofibers (TiO_2 NFs) synthesized by electrospinning. The TiO_2 NFs were coated by atomic layer deposition (ALD) to grow boron nitride (BN) and palladium (Pd) on their surface. The UV-Vis spectroscopy measurements confirmed the increase of the band gap and the extension of the spectral response to the visible range. The obtained TiO_2/BN/Pd nanofibers were then tested for photocatalysis, and showed a drastic increase of acetaminophen (ACT) degradation (>90%), compared to only 20% degradation obtained with pure TiO_2 after 4 h of visible light irradiation. The high photocatalytic activity was attributed to the good dispersion of Pd NPs on TiO_2–BN nanofibers, leading to a higher transfer of photoexcited hole carriers and a decrease of photogenerated electron–charge recombination. To confirm its reusability, recycling tests on the hybrid photocatalyst TiO_2/BN/Pd have been performed, showing a good stability over 5 cycles under UV and visible light. In addition, toxicity tests as well as quenching tests were carried out to check the toxicity of the byproducts formed and to determine active species responsible for the degradation. The results presented in this work demonstrate the potential of TiO_2/BN/Pd nanomaterials, and open new prospects for the preparation of tunable photocatalysts.

Received 2nd November 2021,
Accepted 6th January 2022

DOI: 10.1039/d1dt03715c

rsc.li/dalton

1. Introduction

Water scarcity is a worldwide issue since the demand for clean water highly exceeds freshwater availability.[1] To respond to this high demand, many sources of water have been considered such as wastewater, rainwater and seawater. However, these sources may contain harmful contaminants such as dyes, pesticides, pharmaceuticals and personal products, considered "emerging pollutants".[2] Additionally, conventional wastewater treatment methods are inefficient in removing persistent organic substances such as drugs from the water, and the presence of such contaminants, even at low concentrations, may be harmful to human health and aquatic organisms.[3–5] Many new techniques have been developed to overcome these limitations, such as ozonation, electrooxidation, photo-Fenton processes and photocatalysis.[6,7] Photocatalysis has attracted much attention in the last few

[a]*Institut Européen des Membranes, IEM UMR 5635, Univ Montpellier, CNRS, ENSCM Place Eugène Bataillon, 34095 Montpellier cedex 5, France. E-mail: mikhael.bechelany@umontpellier.fr*
[b]*Laboratoire d'Analyses Chimiques, LAC – Lebanese University, Faculty of Sciences, Jdeidet 90656, Lebanon*
[c]*Department of Analysis and Evaluation, Egyptian Petroleum Research Institute, Cairo, 11727, Egypt*
[d]*NanoBioMedical Centre, Adam Mickiewicz University, Wszechnicy Piastowskiej 3, 61-614 Poznan, Poland*
[e]*Institut of Atomic Physics and Spectroscopy, University of Latvia, Rainis Blvd., LV-1586 Riga, Latvia*
[f]*Center for Collective Use of Scientific Equipment, Sumy State University, 31, Sanatornaya st, 40018 Sumy, Ukraine*
[g]*Univ. Grenoble Alpes, CNRS, Grenoble INP, LMGP, F-38000 Grenoble, France*

†Electronic supplementary information (ESI) available. See DOI: 10.1039/d1dt03715c

decades as a promising approach for water treatment.[8,9] It is an advanced oxidation process, based on the excitation of a semiconductor that will engender electron–hole pairs responsible for the degradation of pollutant.[10,11] Therefore, it is considered as an effective technique to remove trace contaminants and their intermediate products that could be more harmful.[12,13]

In recent years, semiconductor photocatalysts have been considered for environmental and energy applications for catalytic and sensing purposes.[14–16] Among the semiconductors used in photocatalysis, titanium dioxide (TiO_2) has received much attention for the removal of organic pollutants from wastewater. TiO_2 has several advantages regarding its high photocatalytic efficiency, high stability, low toxicity and low cost.[17–19] However, the wide band gap (~3.0–3.2 eV) limits the application of this photocatalyst under visible light. Another disadvantage is the fast recombination of photogenerated carriers, limiting its usage on a large scale.[20–22]

During the last few years, research has focused on designing hybrid nanocatalysts and heterostructures to conquer TiO_2 limitations.[23–26] Many studies have been presented, such as doping with metal ions (Pd, Ag, Pt...),[10,27–30] and nonmetal ions (B, N, Cu, Ni...),[31,32] and creation of heterojunctions with other semiconductors (BN, ZnO, CuO).[33–35] Coupling TiO_2 with other semiconductors or metals will allow the formation of heterojunctions that can increase the lifetime carrier charge, reduce the recombination of electron holes, and improve the photocatalytic efficiency of TiO_2 under visible light.[36,37]

Many studies have reported the efficiency of doping TiO_2 with boron nitride (BN) for dyes and pollutant degradation, since BN has a high ability for energy storage to allow higher e^-–h^+ transfers and a high chemical stability.[38,39] Nasr *et al.* reported that TiO_2–BN nanocomposites synthesized by electrospinning enhanced the degradation of methyl orange under UV light. They confirmed that BN could improve the photocatalytic activity of TiO_2 due to the immigration of holes to the catalyst surface.[10] The photocatalytic oxidation of ibuprofen by TiO_2–BN nanocomposites was also studied by Lin *et al.*[40] The photodegradation of ibuprofen was enhanced due to the incorporation of BN, and a complete degradation was obtained after 2 h of UV irradiation. Sheng *et al.* prepared hexagonal boron nitride (h-BN)/titania (TiO_2) nanocomposites by sol–gel. They reported the degradation of rhodamine B (RhB) and methylene blue (MB) under UV light irradiation of 98% and 92% within 50 min irradiation, respectively.[41]

In addition, loading noble metals such as palladium (Pd), platinum (Pt) and silver (Ag) on the surface of the substrate appears to be effective for the elaboration of potential catalysts.[42,43] These metal nanoparticles (NPs) will allow the improvement of visible light excitation and reduce the recombination of e^-/h^+ pairs due to the surface plasmonic resonance effect and the metals' performance as charge acceptors, respectively.[44] Among these metals, loading Pd on the surface of TiO_2 has proved to be an effective method to improve visible light photocatalytic degradation. Mohapatra *et al.* prepared TiO_2-NTs with well-dispersed Pd NPs by incipient wetness method. The catalyst has shown effective degradation of dyes under solar light simulator.[45] Moreover, photocatalytic oxidation of nitrogen oxide (NO) was successful using Pd-modified TiO_2 prepared by thermal impregnation method.[46]

Most of these studies have used several techniques such as electrospinning,[22] sol–gel method,[47] microwave-assisted synthesis,[48] *etc*. Since visible photocatalysts are required for efficient catalytic applications, a highly structured material with a large specific area and more exposed active sites should be designed.[49] To our knowledge, no degradation of acetaminophen (ACT) was reported with TiO_2–BN–Pd nanocomposites. The major challenge is to design a semiconductor catalyst with a well-known structure, precise morphology and high selectivity. Atomic layer deposition (ALD) combined with electrospinning shows potential advantages in fabricating highly effective and selective photocatalysts.

ALD is a vapor deposition technique that allows the preparation of thin films in the sub-nanometer scale with precise thickness and high conformality.[50,51] ALD enables the synthesis of nanoparticles and thin films with controllable dimensions at the subnanoscale, a unique capability.[52–57] The use of ALD in the catalysis field is getting more attention since it enables the design of nanocatalysts with control over size, composition, thickness and distribution of the material.[58] For example, Weber *et al.* reported the synthesis of carbon paper-boron nitride-palladium electrodes using ALD, the electrochemical active surface of which remained stable even after applying an accelerated ageing program for 1000 cycles.[59]

In their recent review, Vempati *et al.* reported the importance of the combination of ALD with electrospinning in the elaboration of catalytic materials.[60] Electrospinning is an easy technique for preparing NFs with a controlled diameter in a range between 10–1000 nm, by applying a high electric field between the polymeric solution and the collector.[61,62] Preparation of TiO_2 nanofibers by electrospinning has been widely used, since electrospinning allows the preparation of many nanostructures with low aggregation, high porosity, and large specific surface area, which can promote the charge and mass transfer for enhanced photocatalytic activities.[63,64]

Recently, nanocomposite materials for photocatalytic degradation of pharmaceutical pollutants have been the subject of many research studies.[65–67] Herein, we report for the first time the degradation of ACT with TiO_2–BN–Pd catalyst obtained by combining two major techniques, electrospinning and ALD. First, TiO_2 was synthesized by electrospinning, followed by a uniform deposition of BN by ALD. Pd nanoparticles were then added to obtain hybrid catalysts. Moreover, a variation of BN deposition cycles was also performed, and the degradation of ACT, used as a model pollutant, was compared under UV and visible light. The TiO_2–BN100–Pd100 hybrid photocatalyst has shown the best photocatalytic activity among all prepared catalysts. Moreover, the catalyst has shown high stability even after 5 cycles. The toxicity was also evaluated during the degradation process to ensure that harmful byproducts generated during the process were degraded as well. Finally, a scavenger study was conducted to get an idea about the mechanism of degradation of ACT. The main species responsible for the degradation of acetaminophen were holes and superoxide radicals.

2. Experimental

2.1. Materials and chemicals

Titanium(IV) isopropoxide (TTIP, 97%, CAS: 546-68-9), polyvinyl pyrollidone (PVP, M_w = 1 300 000, CAS: 9003-39-8), acetaminophen (ACT, ≥99% CAS: 103-90-2), formaline solution (HCHO, CAS: 50-00-0), boron tribromide (BBr_3, 99,9%, CAS: 10294-33-4), Nafion perfluorinated resin solution (CAS: 31175-20-9), sodium sulfate (Na_2SO_4, ≥99%, CAS: 7757-82-6), sodium chloride (NaCl, ≥99%, CAS: 7647-14-5), 2-propanol (99.9%, CAS: 67-63-0), *p*-benzoquinone ($C_6H_4O_2$, ≥99.5%, CAS: 106-51-4) and ethylenediaminetetraacetic acid (EDTA, 99.995%, CAS: 60-00-4) were purchased from Sigma-Aldrich. In addition, Pd palladium(II) hexafluoroacetylacetonate (≥95%, CAS: 64916-48-9) was purchased from Strem Chemicals. Acetic acid (CAS: 64-19-7) and ethanol (≥99.8% CAS: 64-17-5) were purchased from VWR chemicals and used as solvents. All chemicals were used without further purification. Indium tin oxide (ITO) deposited on quartz was purchased from Präzisions Glas & Optik. Deionized (DI) water (>18.2 MΩ) prepared using a Millipore (Milli-Q® Academic) water purification system was used for all dilutions and reagent preparation. Argon gas and ammonia were bought from Linde and used as received.

2.2. Synthesis of TiO_2 nanofibers by electrospinning

The preparation of TTIP/PVP solution was similar to previous studies as shown in Fig. 1.[19] Acetic acid and ethanol were used as solvents. The suspension was stirred for 2 h prior to spinning in order to increase the dielectric constant and obtain an electrospinnable solution. The resulting solution was then loaded in a 22 mL syringe and electrospun using a homemade electrospinning system. During the process, a high voltage of 25 kV and a flow rate of 1 mL h^{-1} were applied. The distance between the 19 gauge needle and the collector was fixed at 10 cm. When the electric field is created, the polymer jet between the droplet and the grounded collector leads to fibres forming, overcoming the surface forces.[68–70] This process was followed by calcination of obtained fibers at 400 °C for 4 h to remove the polymer and obtain crystalline TiO_2.

2.3. Modification of TiO_2 by atomic layer deposition

2.3.1. Atomic layer deposition of boron nitride. The coating of BN was carried out on electrospun nanofibers at 750 °C in a low-pressure homemade ALD reactor. The reactor was directly connected to the precursor and co-reactant lines through gate valves and heated at 110 °C to avoid condensation. The deposition of BN was achieved using sequential exposures of BBr_3 and NH_3 (considered as co-reactant) separated by purge steps of argon with a flow rate of 100 sccm. One ALD cycle consisted of a 0.1 s BBr_3 pulse, 5 s exposure, and 15 s Ar purge, followed by a 5 s NH_3 pulse, 5 s exposure, and 20 s Ar purge. More details on the ALD reactor and on the process are listed elswhere.[5] In order to adjust the BN loading, the number of ALD cycles was varied. Thicknesses of deposited BN were identified by ellipsometric measurments (Semilab spectroscopic ellipsometer GES5E, Xe lamp 1.23 eV–5 eV). Si substrates were added with NFs during the ALD deposition and the data was fitted using the Cauchy fitting model.

2.3.2. Atomic layer deposition of palladium. TiO_2–Pd was synthesized by atomic layer deposition in a low-pressure hot-

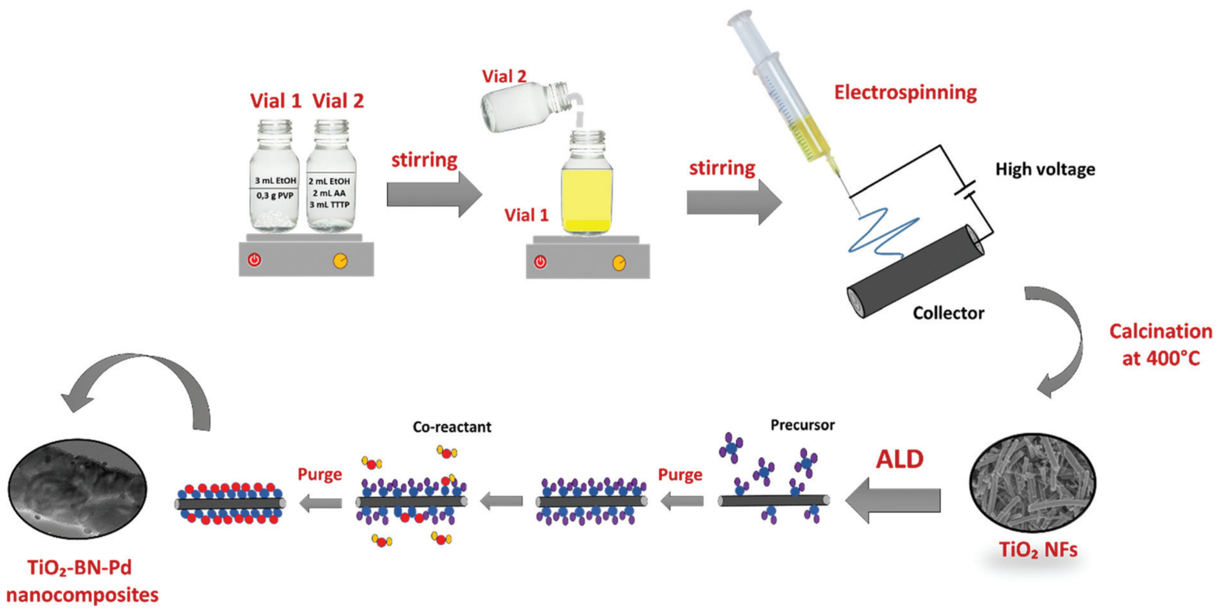

Fig. 1 Illustration of the steps for the preparation of nanocomposites. In the first step we prepared the polymeric solution, then electrospinning was performed. The collected nanofibers were then calcined before the ALD process.

wall (home-built) reactor, described elsewhere.[71,72] ALD of Pd was carried out with $Pd(hfac)_2$ and formalin. The highly dispersed Pd NPs were synthesized by applying 100 ALD cycles. The bubbler containing the $Pd(hfac)_2$ precursor was heated at 70 °C and the formalin container was kept at room temperature. The deposition chamber was set at a temperature of 220 °C, and the lines in the ALD system were heated at 80 °C to avoid any condensation.[73] The ALD cycle consisted of sequential pulse, exposure, and purge of Pd precursor and formalin, alternately. The pulse, exposure, and purge durations were 5 : 15 : 10 s and 1 : 15 : 60 s for $Pd(hfac)_2$ and formalin, respectively.

2.4. Characterization of the synthesized nanocomposites

A Hitachi S4800 emission scanning electron microscope (SEM, JAPAN) was used for morphology measurements of synthesized nanofibers. All samples were sputter coated with platinum/palladium before SEM measurement using a Polaron SC7620 Mini Sputter Coater. The crystal phases of the samples were examined by XRD diffractometer using Cu-Kα radiation (λ = 1.5406 Å) in 2θ ranging from 10 to 80°. Fourier-transform infrared spectroscopy (FTIR) of TiO_2, TiO_2–BN, TiO_2–Pd and TiO_2–BN–Pd nanocomposites was recorded with the NEXUS instrument, equipped with an attenuated total reflection accessory in the frequency range of 400–4000 cm^{-1}. Raman spectra were measured by dispersive Raman spectroscopy (Horiba XploRA), using a 659.55 nm laser and an objective lens of 100. Transmission electron microscopy (TEM) was performed using JEOL 2200FS (200 kV) and JEOL ARM-200F (200 kV). X-ray photoelectron spectroscopy (XPS) measurements were conducted *via* ESCALAB 250 spectrometer from Thermo Electron using Al Kα monochromatic source (1486.6 eV) as an excitation source. In order to determine the band gaps of synthesized materials, the UV–vis spectra were measured using a UV–vis spectrophotometer (Jasco model V570) equipped with a diffuse reflectance (DR) attachment (Shimadzu IRS-2200) for optical absorbance measurements. Photoluminescence (PL) spectra were recorded with an optical fiber spectrometer (Ocean Optics usb2000) with an excitation wavelength of 266 nm using a nitrogen Nd:YAG laser, 9 mW.

2.5. Electrochemical impedance spectroscopy measurement

An electrochemical system was used to carry out the EIS tests using a Solartron SI 1287 potentiostat/galvanostat. Three-electrode cells were used to study the photoelectrochemical property: photocatalysts used as working electrode, Ag/AgCl as reference electrode, and platinum wire as counter electrode, immersed in Na_2SO_4 solution (0.1 mol L^{-1}) considered as electrolyte. The mixtures of 4 mg photocatalyst, 1 mL isopropanol and 40 μL Nafion aqueous solution were homogeneously mixed using the ultrasonic cleaner for 30 min, then the slurry was dropped on the ITO glass (1 × 1 cm), and the working electrode was achieved after the evaporation of isopropanol. Moreover, the measurements were done using a 150 W halogen lamp as the light source under visible light exposition.

2.6. Quantum efficiency measurements

The measurements were performed in the following way:

A 3.5 mL plastic cuvette was filled with 2.5 mL of mQ water and installed into a cuvette holder. A tungsten light source (Avantes) was used for absorbance measurements. The 1 mg mL^{-1} water solutions of TiO_2–X samples were prepared. 50 mL of solution was added to the cuvette and absolute irradiance spectra of the sample were recorded (Fig. S1†).

According to Kubelka–Munk the following equations are applicable for the calculation of quantum efficiency:[74]

$$R_\infty = \frac{\left(1+R_0^2-T^2\right)-\left(\left(1+R_0^2-T^2\right)^2-4R_0^2\right)^{0.5}}{2R_0} \tag{1}$$

where T is transmittance (%) and R_0 is reflectance (%).

Within this theory, absorption and scattering coefficients can be calculated, and the detailed calculation is represented in ESI.†[74]

The quantum efficiency for 1 cm^3 volume of 0.5 mg mL^{-1} photocatalyst solution was calculated as the following eqn (2):

$$\mathrm{QE} = \frac{N_0 - N}{\sum_{400\,\mathrm{nm}}^{700\,\mathrm{nm}} \eta(\lambda)\cdot N_{\mathrm{ph}}(\lambda)} \tag{2}$$

where N_0, N, $\eta(\lambda)$ and $N_{ph}(\lambda)$ are the initial concentration of organic molecules (cm^{-3}), concentration of organic molecules after 3 hours of exposure to visible light (cm^{-3}), part of absorbed light and number of incident photons (cm^{-2}) for wavelength λ.

2.7. Photocatalytic experiments of acetaminophen

Photocatalytic activity of the synthesized nanocomposite was evaluated on the degradation of ACT under two light sources. A medium pressure metal halide UV lamp (400 W, Lampes France) and a visible light source provided by a linear halogen lamp (400 W, Avide) were used for the comparative study. The irradiation distance between the lamp and the sample was fixed to 10 cm for all experiments.

The photocatalysts (0.5 g L^{-1} – TiO_2, TiO_2–BN, TiO_2–Pd and TiO_2–BN–Pd) were added into 250 mL of ACT solution (1 mg L^{-1}) in a 300 mL glass reactor. A water bath was used to minimize the temperature increase in the solution under the light irradiation and keep it stable at 37 °C. The solution was stirred for 30 minutes to ensure equilibrium adsorption in the dark and then exposed to irradiation. At certain time intervals, 3 mL aliquots were sampled and filtered with 0.22 μm filters. The ACT concentration was analyzed by high-performance liquid chromatography equipped with a C-18 column (RP18, Nucleoshell) and a Quattro-Micro mass spectrometer with an Electrospray probe (Waters Micromass, Wythenshawe, Manchester, UK) as a detector. An isocratic method (A/B = 97/3) set at 0.25 mL min^{-1} flow rate was used. The phase A of eluents consisted of a mixture of acetonitrile/water (95/05), while the phase B was 100% acetonitrile with 0.1% formic acid for both phases.

The recyclability of the catalyst that showed the best degradation efficiency was further investigated. The nanocomposite was reused under UV and visible light for 5 cycles with the same initial conditions.

The degradation efficiency ($D(\%)$), was calculated according to eqn (3):

$$D(\%) = [(C_0 - C)/C_0] \times 100 \tag{3}$$

where: C_0 and C are the initial and final concentrations at mg L^{-1}.

2.8. Photocatalytic kinetic model

Typically, TiO_2 kinetics is usually characterized by the Langmuir–Hinshelwood (L–H) model.[40,75] When the concentration of the pollutant is low, pseudo-first-order kinetics is applied,[76] eqn (4):

$$\ln(C_0/C) = kt \tag{4}$$

where C_0 (mg L^{-1}) is the initial concentration of the pollutant, C is the pollutant concentration at time t (min) and k (min^{-1}) is the pseudo-first-order rate constant.

2.9. Microtoxicity tests for determination of byproducts' toxicity

During the degradation of acetaminophen, many byproducts can be formed.[77] In order to confirm or not the toxicity of these compounds, a bioluminescence toxicity study was carried out. This study is based on the measurements of the luminescence effect of marine bacteria. The bacteria used in this method were of the strain *Vibrio fischeri* LCK 487. All measurements were conducted using Microtox® Model 500 Analyzer (Modern Water Inc.; United Kingdom) coupled with MicrotoxOmni® software. First, reconstitution of the bacteria was performed by adding 5 mL of the reagent diluents at 5 °C. Then 200 μL of the solution was transferred to the cuvettes, and the reagent was stabilized at 15 °C for 15 min. In order to enhance the activity of the *Vibrio fischeri* bacteria, the samples were diluted at 81.8% of initial concentration by adding 22% NaCl solution. Based on luminescence intensity, the screening test at 81.8% allowed identification of the samples' toxicity. Bacterial activity could be reduced by the presence of toxic elements that decrease luminescence. Before measuring the bacterial luminescence, all the samples were filtered with 0.2 mm filters to remove any precipitate or solid matter in the solution. The toxicity values are directly relative to the inhibition rate of bacterial activity, calculated as follows in eqn (5):[77,78]

$$Ic_{(t)}(\%) = \left(1 - \frac{\mathrm{LU}_{(t)}}{\mathrm{LU}_{(0)} \times R_{(t)}}\right) \times 100 \tag{5}$$

where $LU_{(t)}$ is the intensity of luminescence emitted by bacteria after t = 15 min of contact with the sample; $LU_{(0)}$: is the initial intensity of luminescence emitted by bacteria before the addition of the sample; $R(t)$: is the corrected term.

Since the luminescence of bacteria decreases over time and under the action of environmental conditions in the absence of toxicity, it is necessary to compensate for the errors due to these factors by taking into account the variability of the luminescence $R(t)$ of the bacteria in a control solution (MilliQ water and NaCl) which gives the LU_0 values. The corrected term is given by eqn (6):

$$R_{(t)} = \frac{\mathrm{LU}_{0_{(t)}}}{\mathrm{LU}_0} \tag{6}$$

where LU_{0_t} is the intensity of luminescence emitted by bacteria after a t = 5 min or t = 15 min of contact with the control solution (MilliQ water and NaCl); and LU_0: is the initial intensity of luminescence emitted by bacteria before the addition of the control solution (MilliQ water and NaCl).

2.10. Quenching tests

Scavenger tests were performed in order to determine the main active species responsible for the degradation of ACT. Benzoquinone, isopropanol and EDTA were added to the solution at 10, 5 and 17 mM, respectively, before switching the light on. The experiments performed were the same as the degradation process; an aliquot was withdrawn at different times and LC-MS-MS detected the concentration of ACT.

3. Results and discussion

3.1. Characterization of synthesized nanocomposites

TiO_2–BN–Pd photocatalysts were prepared in three steps, as illustrated in Fig. 1. In the first step, TiO_2 nanofibers (NFs) were prepared by electrospinning then calcinated at 400 °C under air. Fig. 2 shows the scanning electron microscopy image of TiO_2 NFs after calcination. It can be clearly seen that we have continuous and randomly oriented nanofibers that preserved their morphologies after calcination. In the second step, atomic layer deposition was used to modify the surface of the prepared NFs. First, we coated TiO_2 with a second semiconductor, boron nitride, at 750 °C. To compare the effect of BN, we varied the BN number of cycles (5 and 100 cycles) for a thickness variation with BN having a GPC on Si substrate of 0.8 nm. The as-prepared samples are designated as TiO_2–BN5 and TiO_2–BN100, respectively. In the last step, a deposition of 100 cycles of Pd was processed on pure TiO_2 NFs and TiO_2–BN composites (denoted as TiO_2–Pd100, TiO_2–BN5–Pd100 and TiO_2–BN100–Pd100). The BN coating was used to enhance the separation of charge carriers as for Pd, it was added to allow the shift of band gap in the visible. Nanofibers with diameter range between 50 and 400 nm with length of several microns were obtained.

SEM images of nanocomposites TiO_2–BN5, TiO_2–BN100, TiO_2–Pd100, TiO_2–BN5–Pd100 and TiO_2–BN100–Pd100 (Fig. 2) show that after ALD deposition, the continuous morphology of TiO_2 was maintained. Nevertheless, when BN deposition increased from 5 to 100 cycles, the surface of TiO_2 NFs became rougher.

In order to get a better idea about the cristallinity of the prepared catalysts, XRD analysis was conducted. According to the XRD patterns (Fig. 3a), pure TiO_2 obtained by electrospinning and calcinated at 400 °C shows a major peak at 25.3°, corresponding to anatase (101) plane. Furthermore, a small peak at 27.4° is assigned to rutile (110). XRD peaks at 25.3°, 37.9°, 48.2°, 55.1° and 62.9° 2θ diffraction angles were assigned to anatase (101), (004), (200), (211) and (204) crystal planes, whereas XRD peaks at 27.5°, 36.2°, 41.3°, 44.1°, 54, 4°, and 69.1° were assigned to rutile TiO_2 (110), (101), (103), (100), (211) and (220) crystalline planes.[17]

The concentration of rutile phase was determined using the Spurr equation:

$$F_R = 1/(1 + 0.8[I_A(101)/I_R(110)]) \quad (7)$$

where I_A and I_R are the integrated intensities of the diffraction peaks for anatase (101) and rutile (110) phases, respectively.[79]

The anatase and rutile fractions were calculated for all the prepared samples. TiO_2 NFs was composed from 70.5% anatase phase while the anatase fraction varied for doped samples; the fraction was in a range between 43.6% (TiO_2–BN100) and 67.1% (TiO_2–Pd). The values of the anatase/rutile phase are represented in Table 1. This decrease in anatase rate in TiO_2–BN100 is due to BN deposition at high temperatures (750 °C) where the anatase is no longer stable. Anatase was proved to be the most active phase for photocatalytic degradation due to the lower rates of recombination and higher surface adsorptive capacity of anatase than that of rutile.[80] However, many studies confirmed that a mixture of crystalline phases 30% rutile and 70% anatase makes the best photocatalyst for the oxidation of organics when applied to treat wastewater.[81] Hence, crystallinity is not the only parameter to be considered; many other factors could affect the activity and selectivity of photocatalysts, such as surface structure, surface defects, and surface charge.[82]

In addition, diffraction peaks of Pd species were not depicted. According to the literature, Pd species (Pd^0 or PdO) could not be detected by XRD due to low dopants' concentration, highly dispersed NPs on the support or overlapping of Pd peaks with TiO_2.[83] For BN, the diffraction peak at $2\theta = 26°$ of hexagonal BN related to the (002) direction has not been observed too; it is probably overlapped with the diffraction peak of TiO_2 at the same position.[10] Moreover, the grain sizes of the TiO_2 dominating phase crystals were calculated to be 11.5, 11.6, 23.5, 32.4 nm, 28.2 nm and 35.3 for TiO_2, TiO_2–Pd, TiO_2–BN5, TiO_2–BN100, TiO_2–BN5–Pd100 and TiO_2–BN100–Pd100, respectively, based on the Scherrer equation described below:

$$D = \frac{K\lambda}{\beta \cos \theta} \quad (8)$$

where D is the crystallite size (nm); K is the Scherrer constant, 0.9; λ, is the X-ray wavelength, 0.15406 nm; β is the full-width at the half maximum intensity of the peak, in radians; and θ is the diffraction angle.[84] It can be concluded that the crystallite size increased remarkably when adding BN.

The increase in crystallite size when doping with BN could be due to the incorporation of B/N in the lattice of TiO_2 or to the higher deposition temperature of BN at 750 °C and/or the generation of oxygen vacancies inside the TiO_2 lattice.[85,86] To confirm these results TEM and XPS were performed and are discussed below.

Fig. 3b shows the Raman spectrum of TiO_2, TiO_2–BN5, TiO_2–BN100, TiO_2–Pd, TiO_2–BN5–Pd100 and TiO_2–BN100–Pd100. The Raman active mode revealed the characteristic peaks of both crystalline phases of TiO_2, anatase and rutile, confirming the XRD results. For all samples, we observe peaks corresponding to the active mode of anatase phase at 151 and

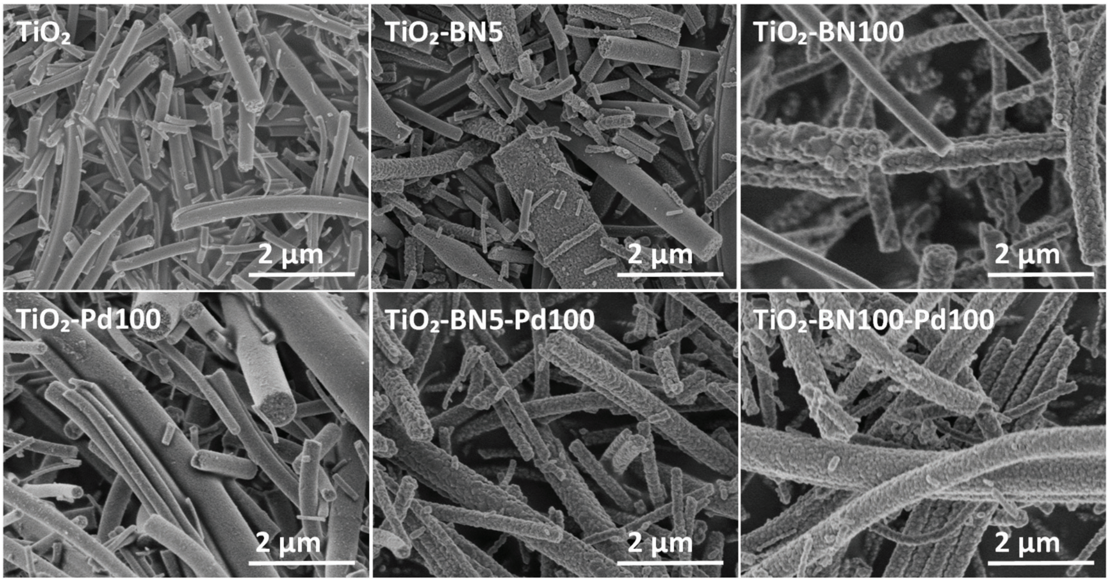

Fig. 2 SEM images of TiO_2, TiO_2–BN5, TiO_2–BN100, TiO_2–Pd100, TiO_2–BN5–Pd100 and TiO_2–BN100–Pd100 nanocomposites.

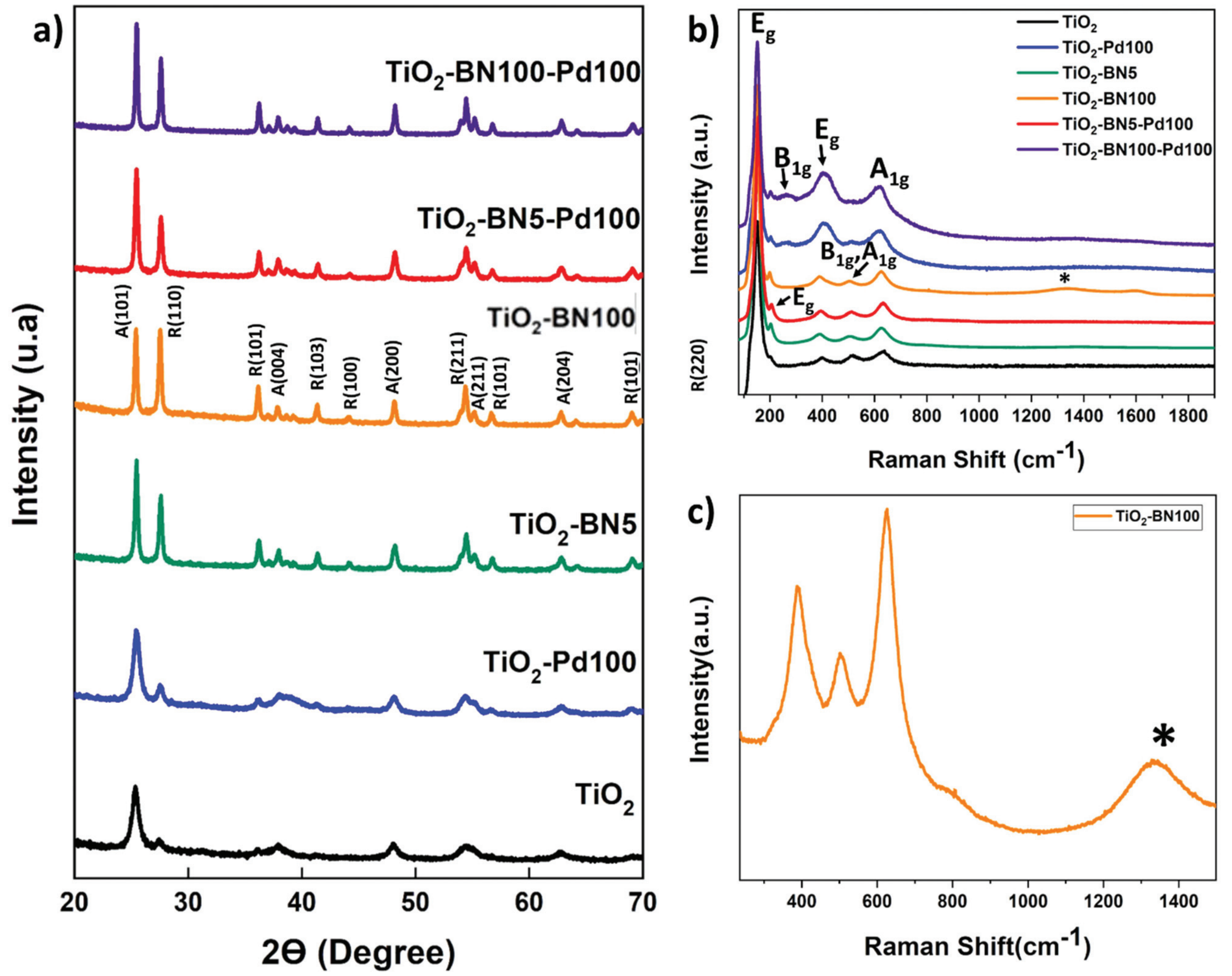

Fig. 3 (a) XRD data (b) Raman spectra of bare TiO_2 and synthesized nanocomposites and (c) zoom on Raman spectra of TiO_2–BN100.

Table 1 Anatase/rutile faction, crystallite size, band gap and QE values of all catalysts

Sample	Anatase (%)	Rutile (%)	Crystallite size (A) (nm)	Band gap (eV)	Quantum Efficiency (%)
TiO_2	70.5	29.5	11.5	3.2 ± 0.01	2.5
TiO_2–Pd100	67.1	32.9	11.6	3.17 ± 0.02	3.6
TiO_2–BN5	53.7	46.2	23.5	3.11 ± 0.03	0.9
TiO_2–BN100	43.6	56.4	32.4	3.11 ± 0.02	1.3
TiO_2–BN5–Pd100	57.2	42.8	28.2	3.10 ± 0.03	12.5
TiO_2–BN100–Pd100	53.4	46.6	35.3	3.09 ± 0.02	21.7

203 (E_g), 513 ($B^1{}_g$, $A^1{}_g$) and 638 (E_g) cm^{-1}. In addition, nanocomposites samples show three peaks corresponding to the active modes of rutile phase at 258 cm^{-1} ($B^1{}_g$), 447 cm^{-1} (E_g) and 633 cm^{-1} ($A^1{}_g$).[12,78] Furthermore, Fig. 3c shows the Raman spectra of TiO_2–BN100, with a small band at 1328 cm^{-1} that could be attributed to h-BN active mode.[87]

In addition to Raman and XRD spectra, infrared spectroscopy was performed to confirm the functional groups of the prepared NFs. Fig. S2† shows the characteristic absorption band of as-prepared samples. The large band at 800–1200 cm^{-1} is attributed to Ti–O bond. For TiO_2–BN100 and TiO_2–BN100–Pd100 in-plane B–N optical mode (1373 cm^{-1}) was observed. No peaks could be detected in TiO_2–BN5 and TiO_2–BN5–Pd100, due to the low amount deposited by ALD (less than 0.5 nm) and/or the incorporation of BN into the lattice of TiO_2.

Since none of the characterization techniques listed above has confirmed the deposition of Pd, high-resolution transmission electron microscopy (HRTEM) was employed. The state of dispersion of metal Pd particles and BN was examined by TEM for TiO_2–Pd100, TiO_2–BN5–Pd100 and TiO_2–BN100–Pd100. TEM images of TiO_2–Pd100, TiO_2–BN5–Pd100 and TiO_2–BN100–Pd100 photocatalysts (to compare the effect of BN, 5 cycles (<0.5 nm) and 100 cycles (~8 nm)) shows that Pd NPs are dispersed uniformly on the surface of TiO_2 NFs. The dispersion of Pd decreases with the increase of BN thickness; this could be explained by the nucleation of the precursor on BN surface and/or the decrease of the nucleation sites. The HRTEM image of Fig. 4c shows that the Pd NPs are deposited on the surface lattice of TiO_2. Mackus *et al.* demonstrated that keeping the sites of TiO_2 catalysts available and depositing particles on preferential sites would enhance the selectivity of the synthesized catalysts.[52] The diameter of Pd NPs was in the range of 1 to 5 nm. In Fig. 5, the boron nitride layer of TiO_2–BN5–Pd100 sample could not be detected by EDX due to the low deposition rate and because boron is a light element that cannot be easily detected by this technique. For TiO_2–BN100–Pd100, Fig. 4i, the HRTEM image indicates that TiO_2 is covered by a layer of ~7 nm of BN. Additionally, Fig. 4f displays the SAED with a lattice spacing of 0.344 nm, which corresponds to the anatase (101), while a *d*-spacing of 0.208 nm is attributed to the Pd (111).

As the obtained TiO_2–BN–Pd nanocomposites were designed and prepared for photocatalytic purposes, it is important to know the chemical state of each element *via* composition analysis using the XPS technique. Fig. S2a† shows the survey spectra of TiO_2–BN100–Pd100; all elements were clearly seen. Fig. 6a shows the Ti 2p XPS spectra of pure TiO_2, TiO_2–

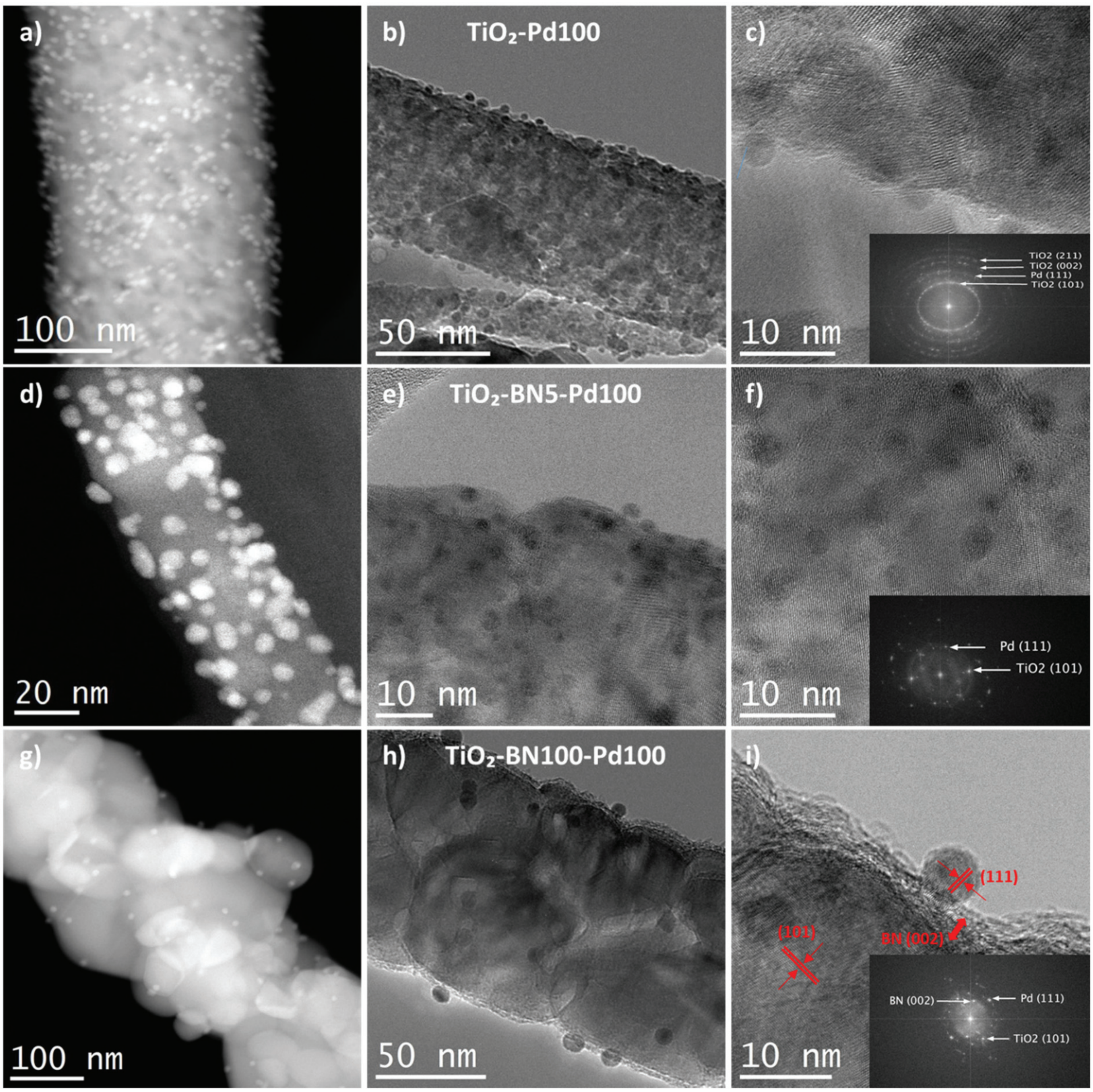

Fig. 4 TEM and HRTEM images of (a–c) TiO_2–Pd100; (d–f) TiO_2–BN5–Pd100 and (g–i) TiO_2–BN100–Pd100.

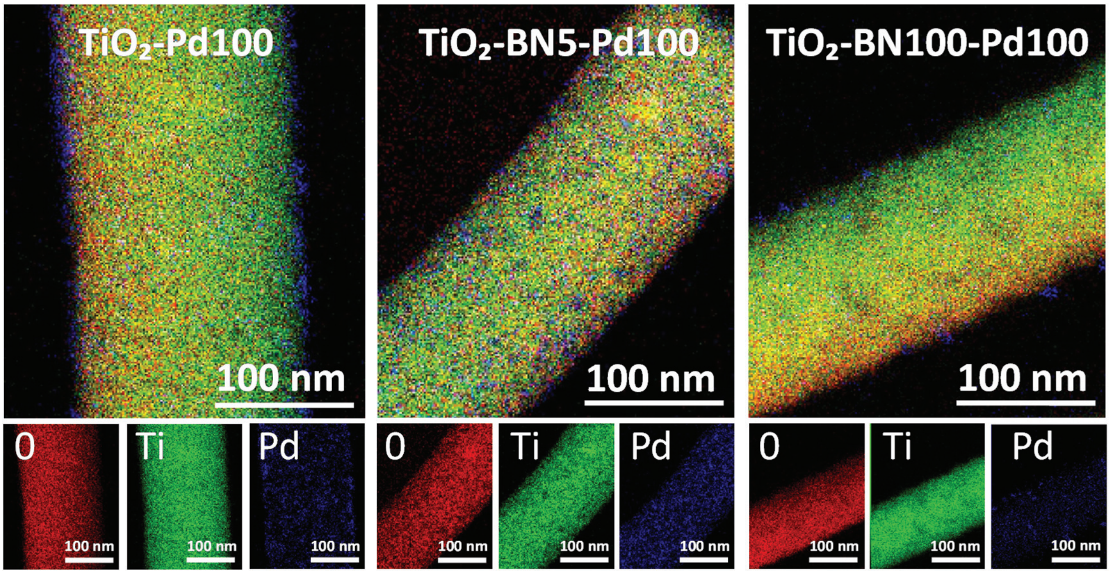

Fig. 5 EDS elemental mapping of TiO_2–Pd100, TiO_2–BN5–Pd100 and TiO_2–BN100–Pd100 nanofibers.

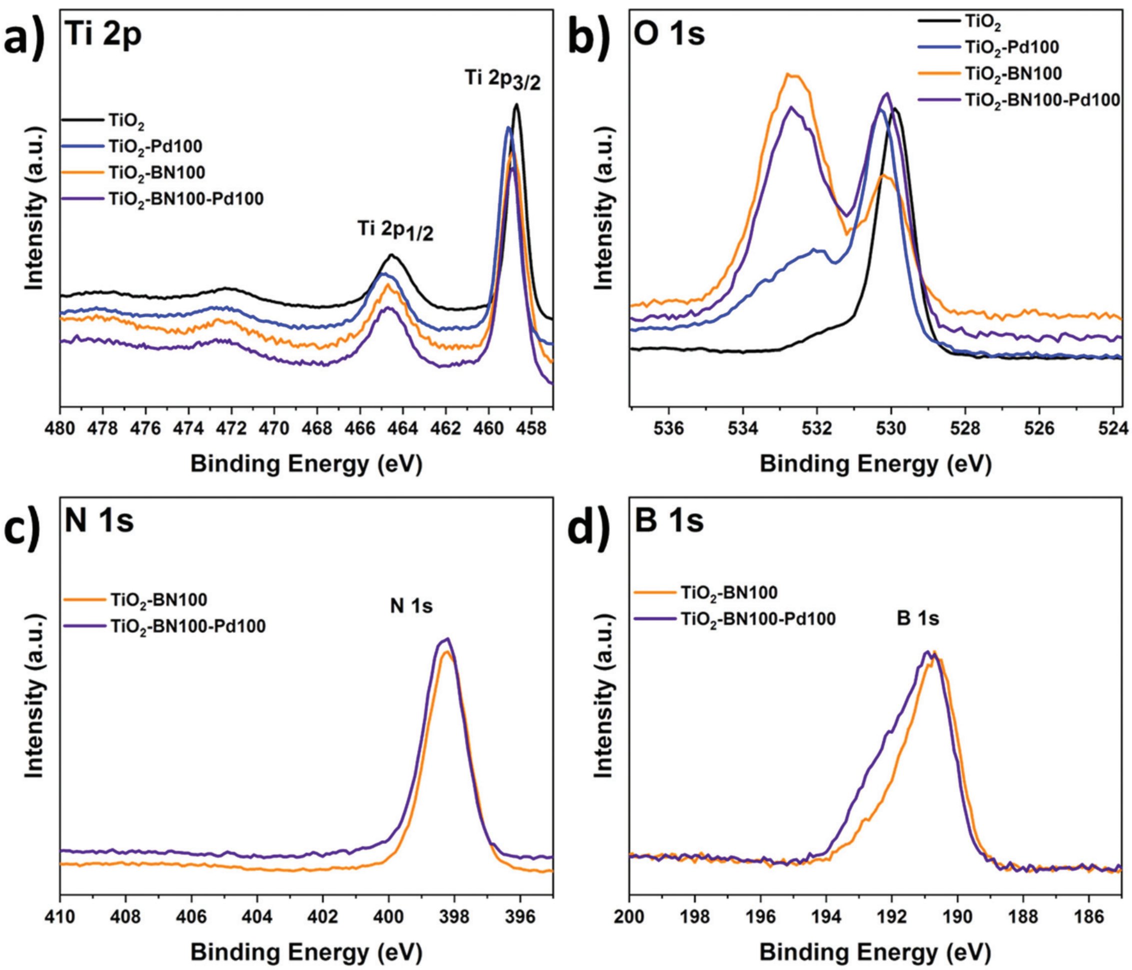

Fig. 6 XPS data of (a) Ti 2p (b) O 1s (c) N 1s and B 1s of all prepared samples.

BN100, TiO_2–Pd100, TiO_2–BN5–Pd100 and TiO_2–BN100–Pd100 composites. For Ti 2p in the TiO_2 sample, two peaks are positioned at 458.7 and 464.4 eV, corresponding to Ti $2p_{3/2}$ and Ti $2p_{1/2}$ states indicating that Ti is 4+ valence. For the TiO_2–BN and TiO_2–Pd samples, Ti 2p peaks are slightly shifted toward higher binding energy (+0.2 eV and +0.3 eV) due to the inclusion of BN and Pd, respectively, into the TiO_2 lattice and the formation of oxygen vacancies exhibiting a high electron-attracting effect.[88] Similar behavior was observed for O 1s spectrum (Fig. 6b). Considering the TiO_2 spectrum as reference, O 1s spectra of TiO_2 show a peak at 529.9 eV attributed to the Ti–O bond, while TiO_2–BN100–Pd100 shows two characteristic peaks at a higher binding energy 530.1 eV attributed to Ti–O bonds and at 532.6 corresponding to B–O–Ti groups. Fig. S3b† shows the deconvolution peaks of O 1s element for all samples. Doping TiO_2 with BN and Pd reduced the atomic percentage of Ti–O–Ti and generated new boron nitride bonds in the case of TiO_2–BN100 and more OH groups in the case of TiO_2–Pd100. For the samples with BN coating (Fig. 6c and d), the B 1s and N 1s elements are identified. The peaks' position of B 1s and N 1s are shifted to higher binding energy when incorporating Pd NPs.

As shown in Fig. 7a, the B 1s spectra consist of peaks at the binding energies of 190.5, 191.5 and 192.6 eV assigned to the edge or interfacial boron bonds connected with –N, –OH and –OTi, respectively. The presence of B–O–Ti bonds can also be proved by the O 1s spectra (Fig. S5†) which is consigned to the formation of a chemical B–O–Ti bond between TiO_2 and boron at the edge of TiO_2.[4] For the TiO_2–BN100–Pd100 sample, the B–OH peak was not noticeable due to the incorporation of Pd NPs on the BN surface. In Fig. 7b the N 1s deconvolution peaks of the TiO_2–BN100 composite revealed the presence of two peaks with binding energy at 398.2 and 398.6 eV ascribed to B–N linkages with Ti–O and the presence of oxidized nitrogen such as N–O–Ti.[88] The atomic percentage and binding energy of all the elements obtained by XPS are listed in Table S1.†

Deconvolution of the XPS spectrum was performed to further understand the incorporation of Pd NPs in the prepared samples. From Fig. 7e and f, two peaks at 335.5 and 340.6 eV were assigned to Pd $3d_{5/2}$ and Pd $3d_{3/2}$. Deconvoluted spectrum of Pd in sample TiO_2–Pd100 and TiO_2–BN100–Pd100 was applied and the main species was found to be Pd^0 for all samples. Composite samples with BN and Pd show an increase of oxidized Pd species, including PdO. This increase could be assigned to a higher Pd oxidation state on the sample's surface, even at low concentrations. Furthermore, the slight increase of oxidized Pd species in the TiO_2–BN–Pd material in comparison with TiO_2–Pd might be explained by the fact that boron nitride attracts electrons from Pd.[89]

The optical properties of pure TiO_2 NFs and TiO_2 composite nanofibers were obtained by UV-Vis absorption spectroscopy measurement. Fig. 8a indicates that TiO_2 NFs absorbs light at 378 nm corresponding to a band gap of 3.2 ± 0.01 eV. For TiO_2 nanocomposite fibers, the absorption edges are red-shifted with the energy of 3.17 ± 0.02, 3.11 ± 0.03, 3.11 ± 0.02, 3.10 ± 0.03 and 3.09 ± 0.02, corresponding to TiO_2–Pd100, TiO_2–BN5, TiO_2–BN100, TiO_2–BN5–Pd and TiO_2–BN100–Pd, respectively. Moreover, all nanocomposite samples have another absorption edge in the visible range. The observed broad absorption peak was observed in the range of 400–580 nm, centered at 540–550 nm. Decrease of the band gap value in TiO_2/BN samples has been reported previously.[10] The redshift of the band gap and increase of visible absorption in BN samples could be explained by formation of new defect states at the BN/TiO_2 interface. Formation of Pd–TiO_2 composite resulted in redshift of the band gap and increase of the visible absorption. This can be ascribed to the improved visible light absorption of M/TiO_2 triggered by the surface plasmon resonance (SPR) of noble metal nanoparticles.[90,91]

The photoluminescence (PL) spectra of the samples are shown in Fig. 8b. Typically to TiO_2-based nanostructures, the intensity of the PL was low (quantum efficiency of TiO_2 ~0.005–0.01). All samples showed a wide peak, centered at 480 nm. The wide peak of prepared TiO_2 nanostructures could be split into two peaks, located at 476 and 573 nm (Fig. 8c). These peaks correspond to self-trapped excitons and oxygen vacancies, respectively.[17,92] Modification of TiO_2 with Pd and BN nanostructures resulted in decreasing the PL. The lowest PL was observed for TiO_2–BN100–Pd100, pointing to higher charge separation rate. Photoluminescence of BN/TiO_2 was studied and explained by Nasr *et al.*[10] Small concentrations of BN did not change PL, whereas high BN concentrations (5–10%) reduced PL intensity by 2 times. In addition, photoluminescence intensity decreased in samples with Pd due to the formation of a Schottky barrier between Pd and TiO_2.[93] Thus, Pd and BN act as additional quenching factors of PL. Values of the quantum efficiency test are presented in Table 1. It should be noted that the yields reported by others cannot be directly compared as there are differences in reactor systems, source of irradiation, volume and concentration of the catalyst.[94] The apparent quantum yield is a parameter which is usually defined as the ratio of converted reactant molecules over the number of photons entering the reactor. A metal oxide material such as TiO_2 (anatase and/or rutile) could never absorb all the incident photon flow from a given source, which can affect the calculation of QE.[95] The values of absorption and scattering coefficients are represented in Fig. S4.† As shown in Table 1, higher quantum yield efficiency was attributed to the TiO_2–BN–Pd nanocomposite, which the higher ACT degradation can explain.

The charge transfer resistance of the photogenerated carriers is investigated through EIS experiments. Fig. 8d shows the Nyquist diagrams of pristine TiO_2 and modified TiO_2 samples. It was found that the diameters of the semicircle decreased in the doped samples with Pd or BN–Pd and the lower value was obtained with TiO_2–BN100–Pd100 nanocomposites. The smaller EIS radius demonstrates the weaker electronic impedance and higher separation of photogenerated electron–hole pairs. This phenomenon benefits from the electronic band structure formed when TiO_2 is doped with BN and Pd, and through this structure, the ultimate catalytic activities

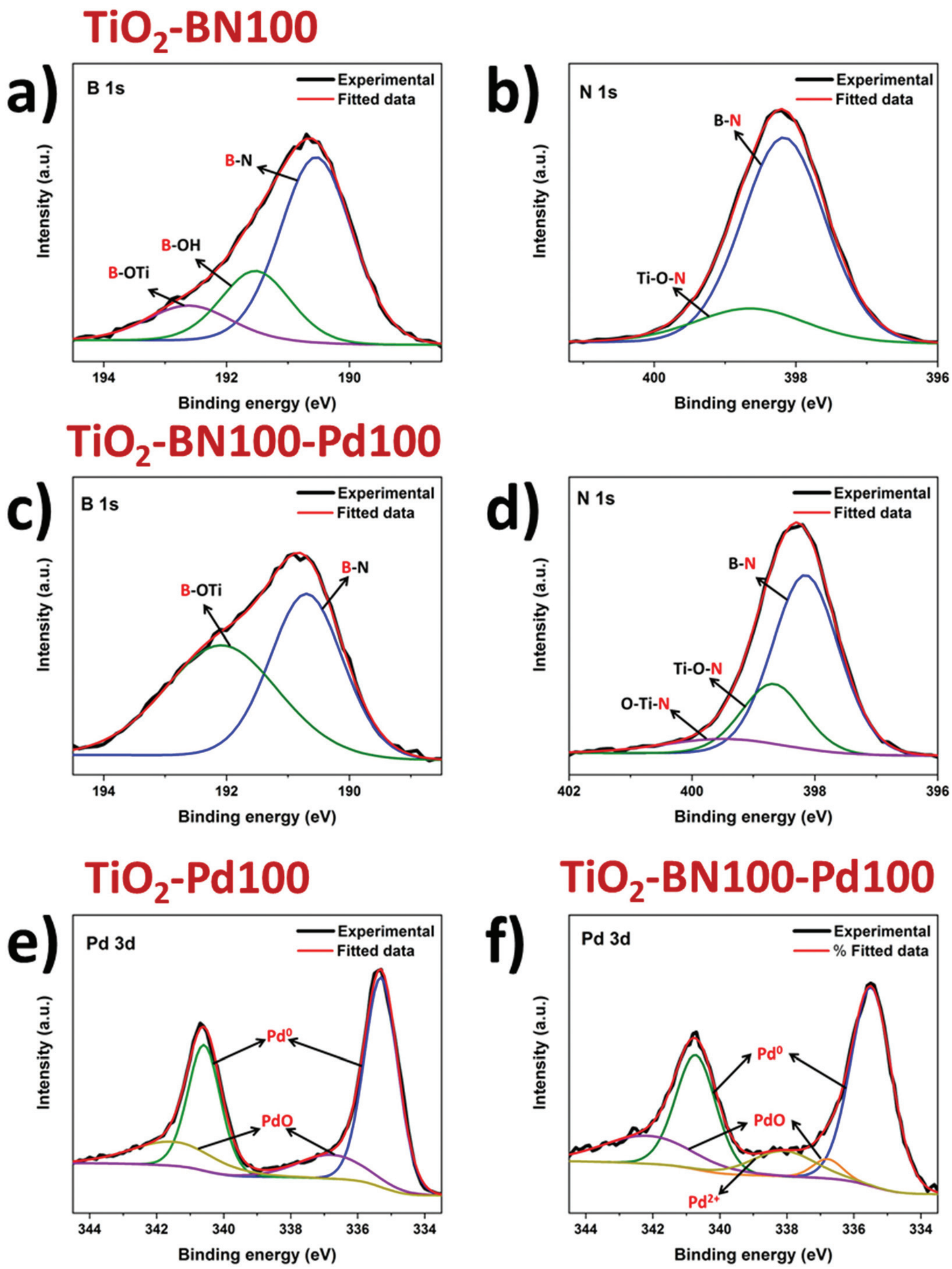

Fig. 7 Deconvoluted XPS spectra of B 1s (a and c), N 1s (b and d) and Pd 3d (e and f) for modified TiO_2 by ALD.

can be promoted. Moreover, Table 2 shows that the smallest polarization resistances are obtained on TiO_2–BN100–Pd100, where R1 represents the bulk resistance of electrodes and electrolyte, R_2 denotes the resistance formed at the nanofibers and electrolyte and Q_2 designates the double layer capacitance at the nanofibers and the electrolyte interface. The lowest R_2 was attributed to TiO_2–BN100–Pd100 nanocomposites with a value of 3.74 KΩ, which refers to a lower resistance between fibers and electrolyte interface. TiO_2–BN100–Pd100 possesses a higher charge transfer rate and a better separation of photogenerated electron–hole than the other prepared catalysts, which has good correlation with the degradation results.

3.2. Photocatalytic degradation

In order to evaluate the modification of TiO_2 surface by ALD, the photocatalytic performance of TiO_2 nanofibers with

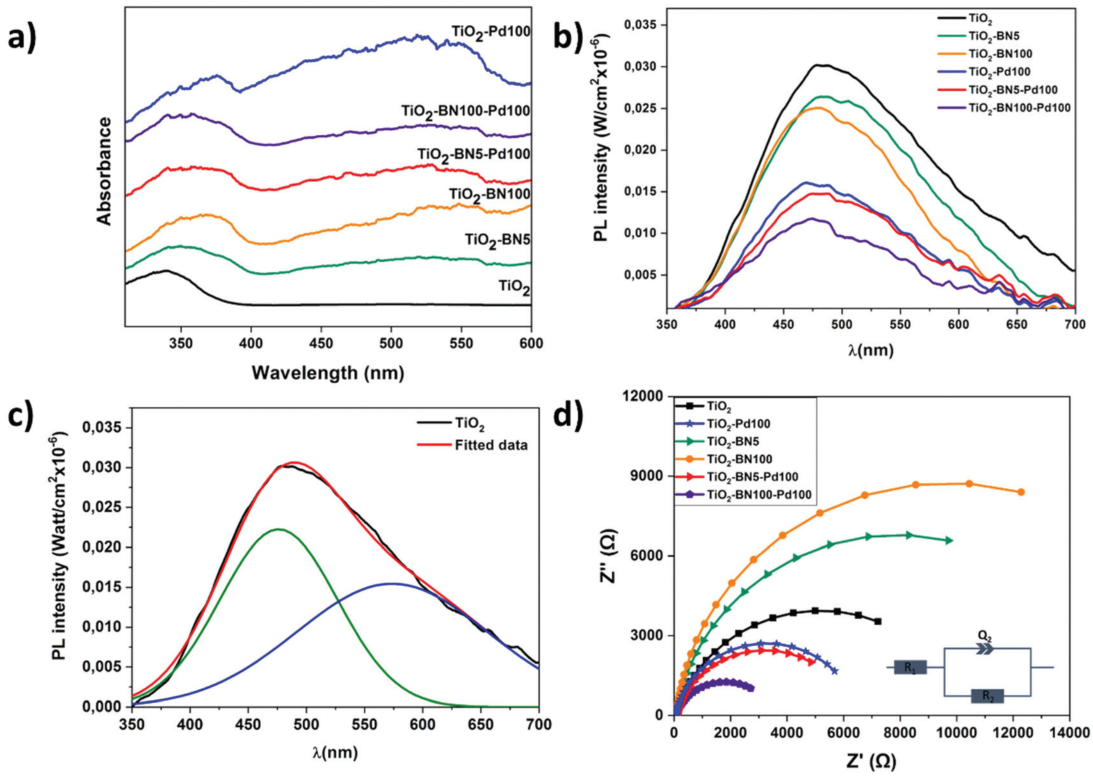

Fig. 8 (a) UV-Vis diffused reflectance of TiO_2 NFs and nanocomposites; (b) photoluminescence of all synthesized NFs; (c) deconvolution of TiO_2 PL spectra; and (d) EIS Nyquist plots of prepared nanofibers.

Table 2 Resistance values from EIS of all synthesized nanofibers

Sample	R_1 (Ω)	R_2 (KΩ)
TiO_2	64.34	10.22
TiO_2–Pd100	65.56	6.44
TiO_2–BN5	76.88	15.86
TiO_2–BN100	83.17	19.82
TiO_2–BN5–Pd100	70.29	6.26
TiO_2–BN100–Pd100	63.66	3.74

different amounts of Pd and BN was evaluated by degrading ACT in ultrapure water under UV and visible light. Fig. 10a and b shows the degradation of ACT under UV light. Herein, the degradation rate was determined by LC-MS-MS every 5 minutes. It can be seen that the degradation with TiO_2–BN–Pd was faster than TiO_2. A total degradation of ACT was reached in less than 15 minutes with TiO_2–Pd100, TiO_2–BN5–Pd00 and TiO_2–BN100–Pd100 with a degradation rate of ACT corresponding to 0.06 mg L^{-1} min^{-1} under UV irradiation. The optimal Pd content was determined by the variation of ALD cycles from 50 to 200 (Fig. S6†). The degradation of ACT was highly affected by the % of Pd content, which is in good agreement with the literature.[96] Higher degradation efficiency was obtained after adding 100 cycles of Pd. For TiO_2 catalyst, the process took 60 min until the degradation was complete. Hence when adding BN, the degradation efficiency decreased. Based on the literature, the deposition of BN by ALD on the surface of TiO_2 can block the active sites on the surface of TiO_2. This can be true when the coverage of TiO_2 is excessive (100 cycles BN). For BN 5 cycles, the effect could be attributed to the more negative valence of BN than TiO_2, which may improve the separation of charge carriers but may be more vital for degradation efficiency. Another reason could be the fact that BN nanosheets adsorb hydrophilic molecules from water less effectively due to its hydrophobic surface.[97,98] This is why elaboration of nanocomposite samples by adding Pd NPs on TiO_2–BN samples was necessary. The formation of heterojunctions in the presence of both BN and Pd at the same time has shown an efficient degradation under UV and visible light due to the enhancement of separation of electron–hole pairs as shown by PL and EIS results.

After 30 min in the dark, equilibrium was reached. Fig. 9a–c shows that the degradation of ACT by TiO_2–BN–Pd was faster than pristine TiO_2. The degradation of the pollutant reached 87% with TiO_2–BN100–Pd100 after 2 h of visible irradiation comparing to just 20% with TiO_2 not modified (Fig. 9b). Furthermore, it can be clearly seen that when we add the Pd, the degradation efficiency increases, and after 4 hours of irradiation, 100% of the pollutant was degraded. The degradation speed of ACT using TiO_2–BN100–Pd100 under visible irradiation after 4 hours was 0.004 mg L^{-1} min^{-1}. This confirms that the Pd has shifted the band gap of TiO_2 to the visible range (confirmed by UV reflectance results), thus

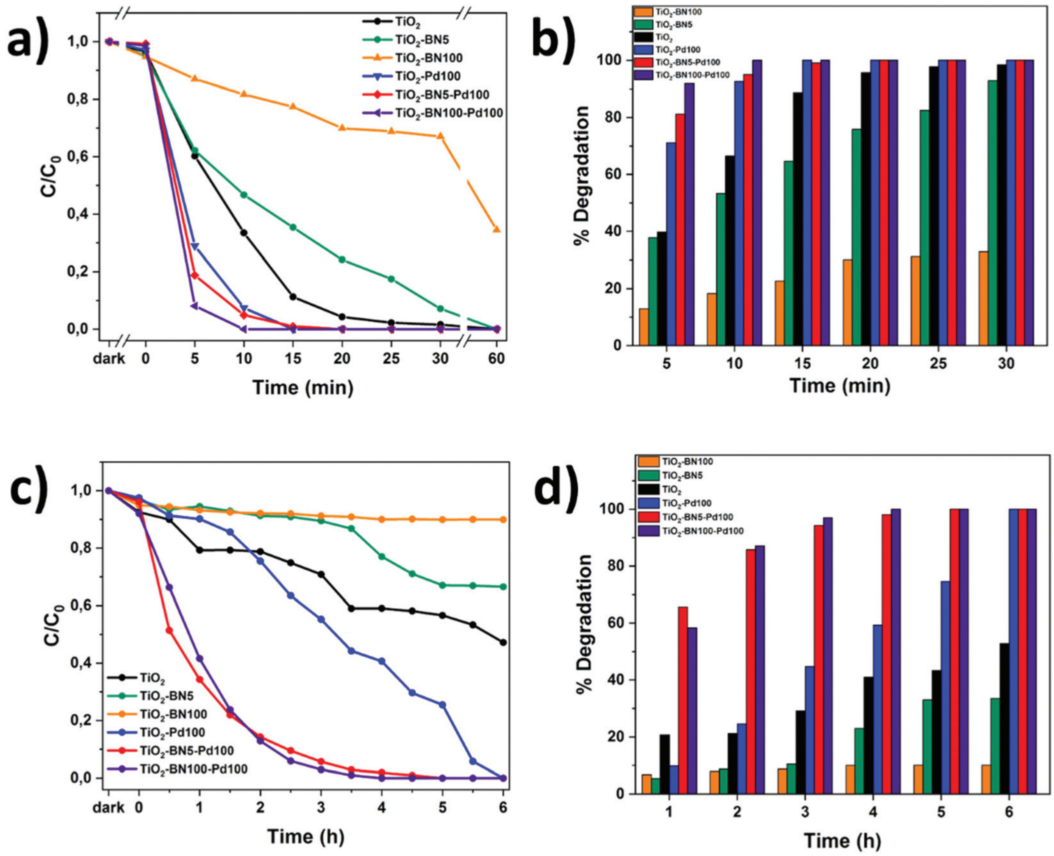

Fig. 9 All prepared catalysts were decomposition of ACT and degradation percentage under (a and b) UV and (c and d) visible light irradiation. Each experiment was conducted at least three times with relative errors of less than 5%.

improving the catalytic activity under visible light.[47] Moreover, Fig. 9d showed that when using TiO_2–Pd100 as a photocatalyst, the degradation has slightly improved compared to TiO_2 after 2 hours. A degradation percentage of 24% *versus* 21% was obtained. After 6 hours, the nanocomposite has led to a total degradation of ACT in comparison with pure TiO_2 that had degraded only 50% of the pollutant. Doping with noble metals like Pd is an effective method to improve the photocatalytic efficiency of TiO_2 as this increases its visible-light capacity. When comparing TiO_2–BN–Pd nanocomposites and TiO_2–Pd, the degradation of ACT was enhanced with TiO_2–BN–Pd. Singh *et al.* have already confirmed that heterojunction engineering promoted charge transfer and enhanced photocatalytic activities of photocatalysts.[99] This could be explained by the formation of Schottky junctions at the interface of noble metal nanoparticles and the semiconductor. The addition of Pd nanoparticles onto the TiO_2–BN surface improves UV-visible light degradation of TiO_2 and creates Schottky junctions, which reduces the recombination of photogenerated carriers in TiO_2.[100] Moreover, TiO_2–BN100–Pd100 showed a better degradation efficiency than TiO_2–BN5–Pd100, and this is due to the lower amount of Pd deposited on TiO_2–BN100 as confirmed by TEM images. It was found that excess Pd loading could decrease the performance of the catalyst. Moreover, Leong *et al.* demonstrated that the synergistic effects of the –O–Pd–O– surface species are mainly responsible for the enhanced photocatalytic activity, which confirms our findings since TiO_2–BN100–Pd100 possesses a higher % of Pd–O than TiO_2–BN5–Pd100 confirmed by deconvoluted XPS data.[101]

The kinetic behavior of the as-prepared catalysts was also investigated under both lights. The photodegradation reactions follow a pseudo-first-order reaction.[33] Fig. 10a–c shows the linear dependence between $\ln(C_0/C)$ and time. The degradation rate increased as follows: TiO_2–BN100 < TiO_2–BN5 < TiO_2 < TiO_2–Pd100 < TiO_2–BN5–Pd100 < TiO_2–BN100–Pd100 under visible light as shown in Fig. 11b. The degradation rate of TiO_2–BN100–Pd100 nanocomposite is 9 times higher than TiO_2 nanofibers under visible light and almost 2 times higher under UV light. These results confirm the role played by heterojunctions between TiO_2, BN and Pd in enhancing the degradation of ACT under visible light. Palladium decreases the band gap of TiO_2, as confirmed by UV reflectance and photoluminescence results, leading to a higher degradation in the visible range, while BN improves the separation efficiency of electron–holes (confirmed by PL results). The increase of photocatalytic degradation of ACT in the presence of BN and Pd could be attributed to the fast transfer of photogenerated electrons from the semiconductor (BN) to the metal NPs (Pd),

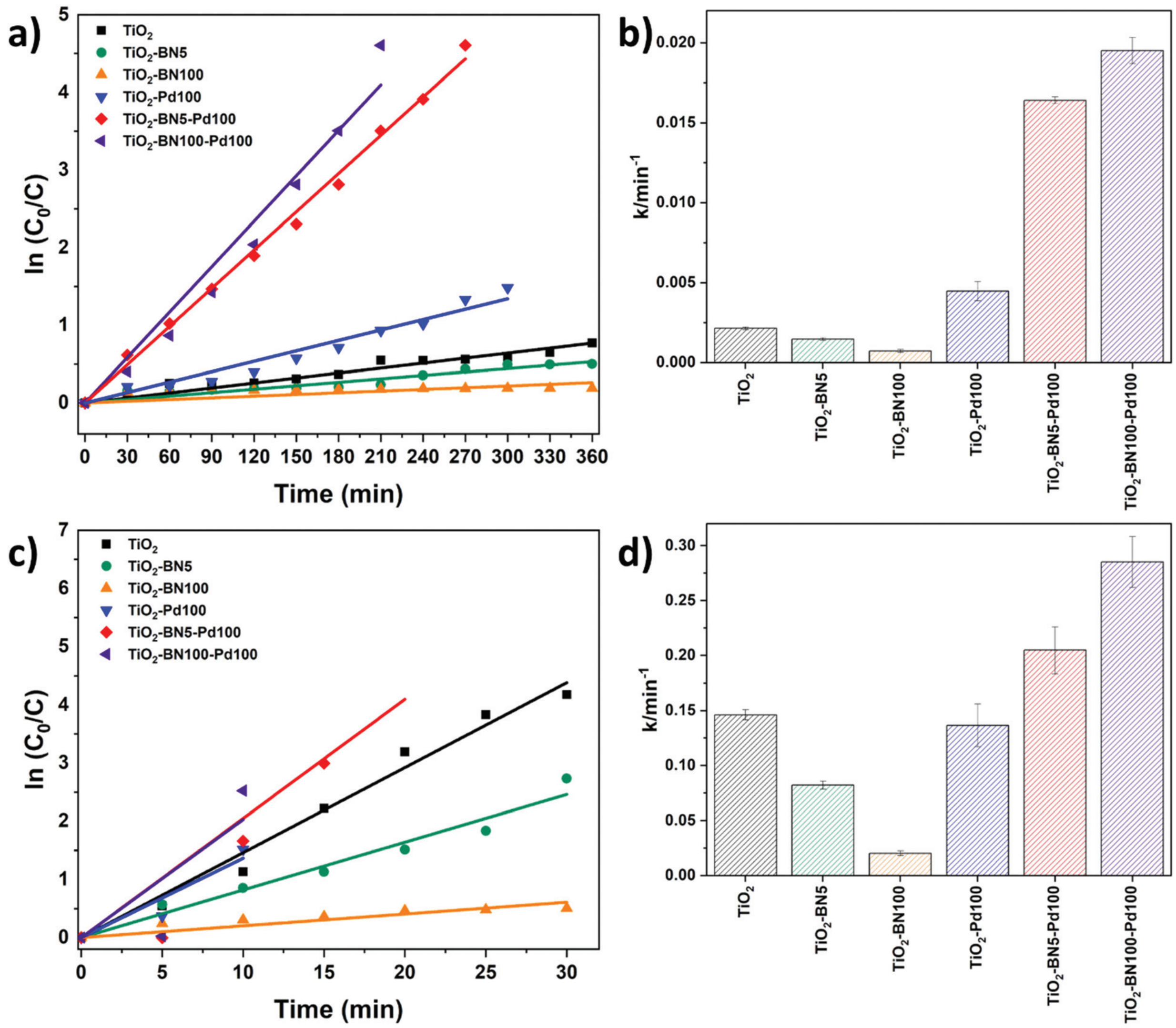

Fig. 10 Kinetics models and rate constant values of ACT degradation under (a and b) UV and (c and d) visible irradiation, respectively. All experiments were conducted at least three times and relative errors were less than 5%.

which enhances the separation of the electrons and holes. Moreover, the shift in optical absorption of the catalyst in the visible region is attributed to the Pd loading and the formation of B–O–Ti bond. This leads to an energy rearrangement that will affect the charge balance. Hence, the band gap of TiO_2–BN–Pd is narrowed and the excited wavelength is extended from UV to visible light region.[44,101,102]

Since TiO_2–BN100–Pd100 nanocomposites have shown the best degradation efficiency, a stability test was performed to confirm the reusability of the catalyst. After each cycle, the catalyst was filtered, washed with deionized water, dried at 100 °C then reused with no further steps. In Fig. 11a, the degradation of ACT remained unchanged under visible light after 5 cycles. For UV irradiation, the degradation efficiency dropped by less than 5% after the second cycle, but remained almost stable until the fifth cycle (Fig. 11b). This reveals that using ALD allows maximising the metal-support interaction, increasing the active sites, and improving the catalyst's stability. The prepared catalyst remains stable and can be reused to degrade water pollutants, thus confirming the advantage of atomic layer deposition in the photocatalytic field.

All further tests were done on TiO_2–BN100–Pd100 nanocomposites. It is known that three main active species can participate in the catalytic process. In order to understand the mechanism of the degradation of ACT by the catalyst, trapping experiments were carried out. Ethylenediaminetetracetate (EDTA), *p*-benzoquinone (*p*-BQ) and isopropanol (IPA) were used as trapping reagents for holes (h^+), superoxide radicals ($^{\bullet}O_2^-$) and hydroxyl radicals ($^{\bullet}OH$), respectively. Fig. 11c shows that the degradation efficiency has clearly decreased from 100% to less than 20% when adding *p*-BQ and EDTA, while it remains almost unchanged when adding IPA under both UV and visible light, showing that $^{\bullet}OH$ do not contribute in the degradation. However, $^{\bullet}O_2^-$ and h^+ both play a major role in

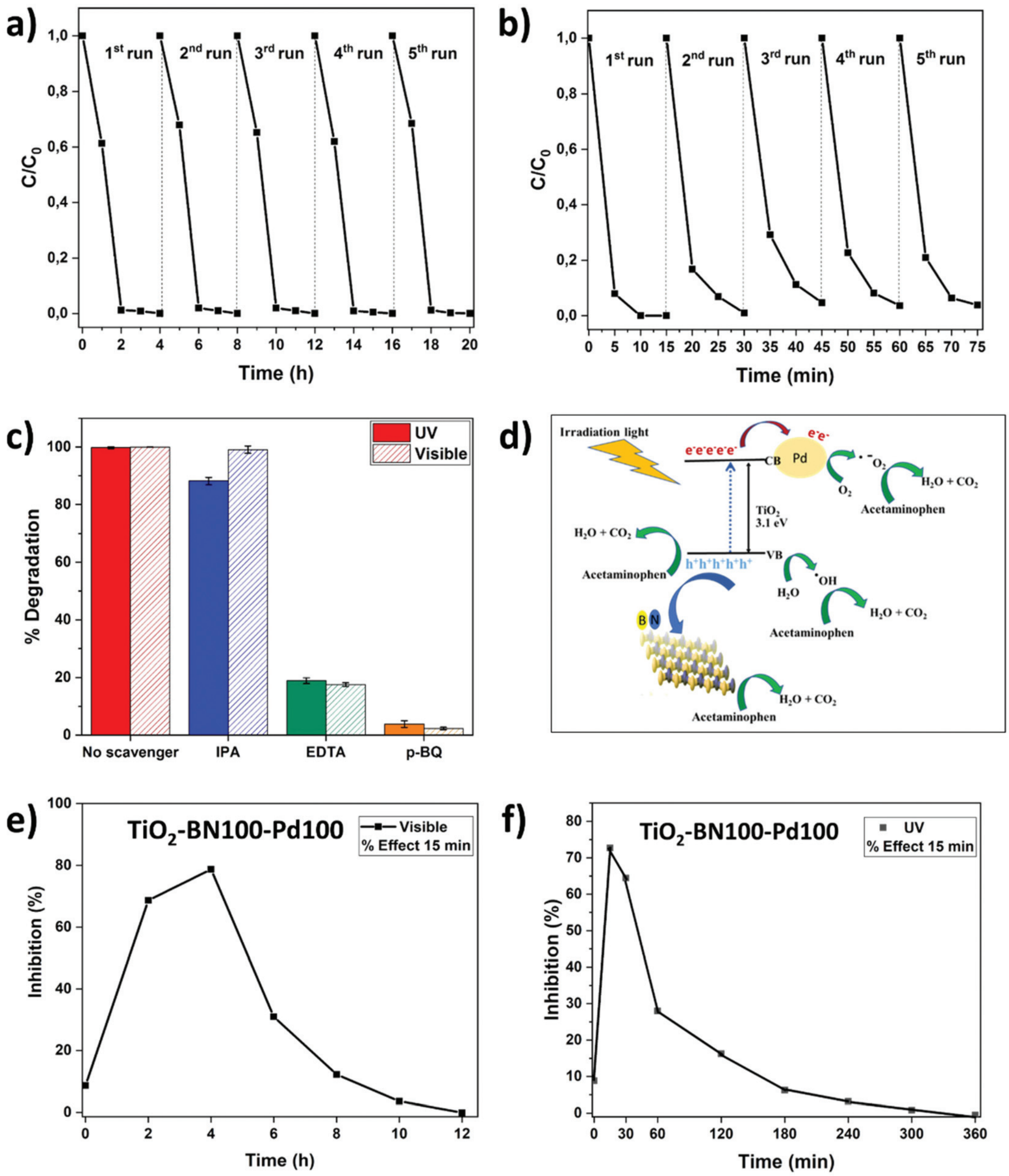

Fig. 11 Recycling test of TiO_2–BN100–Pd100 under (a) visible and (b) UV irradiation; (c) scavenger plot for determining reactive species in the degradation of ACT by TiO_2–BN100–Pd100; (d) mechanism of ACT degradation by TiO_2–BN100–Pd100; inhibition of luminescence of *V. fischeri* marine bacteria during ACT photocatalysis after 15 min exposure between the bacterial strain and the degradation solution under (e) visible and (f) UV irradiation.

the photocatalytic degradation of ACT. The proposed mechanism for the production of oxidants and degradation of acetaminophen molecules is illustrated in the schematic diagram presented in Fig. 11d (mechanism of ACT degradation using TiO_2–BN100–Pd100 nanofibers).[6,103,104] BN, which is negatively charged, acts as a center of attraction for positive holes generated on the surface of TiO_2. This phenomenon will allow slower recombination of electron holes on the surface of TiO_2. Pd NPs with a Fermi level lower than that of TiO_2 will act as traps for photogenerated electrons, which will favor the generation of reactive oxygen species such as hydroxyl and superoxide radicals. The metal deposition on TiO_2 surface allows the separation of electron/holes as well as the separation of sites for photooxido-reduction reactions.[30,105]

3.3. Toxicity tests

Identification of ACT intermediates and their metabolic pathways is essential to evaluate their potential impacts on human health, the environment and aquatic life forms. In this work, we found that $^{\bullet}O_2^-$ and h^+ are the active species in the photocatalytic degradation of ACT, and this agrees with previously published results.[106] Zhang *et al.* suggested the degradation of

Table 3 Comparison of degradation efficiency of differently prepared photocatalysts

Pollutant	$C_{Pollutant}$ (mg L^{-1})	Photocatalyst	$C_{Catalyst}$ (g L^{-1})	Type of irradiation	Energy (W m^{-2})	Degradation time (min)	pH	Removal efficiency (%)	Ref.
ACT	1	TiO_2–BN100–Pd100	0.5	Medium pressure metal halide UV	NA	10	6.8	100	In this work
ACT	1	TiO_2–BN100–Pd100	0.5	Halogen linear lamp	NA	180	6.8	98	In this work
ACT	20	Pt–TiO_2	0.4	Solar irradiation	500	180	6.3	100	109
ACT	20	Degussa P25	2	UV irradiation 365nm	NA	60	NA	98	110
ACT	0.08	TiO_2–Ag5%	1	UV irradiation 365nm	NA	180	NA	98	111
ACT	15	$K_2S_2O_8$–TiO_2	2	Visible irradiation LED lamps	168.5	390	6.9	93	112
MO	10	10%BN/TiO_2 NFs	0.4	UV irradiation	NA	75	NA	99	10
MB	10	BN/TiO_2 composite	0.33	Visible light	NA	200	NA	79	4
RhB	10	12 wt% BN/TiO_2	0.5	Visible-light Xe lamp	1000	150	NA	99	113
ACT	10	MWCNT10%–TiO_2–SiO_2	NA	Visible irradiation high pressure mercury lamp	73.1–75.3	60	7	81.6	114
ACT	30	Fe_2O_3–TiO_2	0.25	Solar simulator halogen lamp	140	180	8	94.8	115
ACT	5	$BaTiO_3$/TiO_2 (3 : 1)	1	UV/Vis xenon lamp	NA	240	7	95	116
ACT	50	TiO_2@rGO TG_3	2	UVA/LED	950	50	5.4	100	117
RhB	10	12% h-BN/TiO_2	0.75	Visible light	NA	120	NA	95	11
ACT	5	3% (w/w) WO_3/TiO_2/SiO_2	1.5	Xenon lamp	NA	360	9	95	118
ACT	18	TiO_2–NFs–SSF	NA	UV light Blue lamps	27	200	6–7	40	119
MB	2	5%Pd/TiO_2	NA	Visible white light	4	1500	NA	10	102
AMX	20	Pd/TiO_2	4	Visible light tungsten	NA	300	NA	97.5	101

ACT *via* two routes: direct holes oxidation and formation of hydroxyl radicals. First, oxidation of holes will lead to the formation of phenolic radicals that will lose their proton and generate superoxide radicals. These radicals will react with phenoxy molecules and generate hydroquinone and 1,4-benzoquinone. The hydroxylation reaction can occur on atom C6 or C7 of the ACT molecule and produce dihydroxyphenyl acetamide. Further oxidation of the formed molecules would result in the breakdown of their aromatic structures followed by the formation of carboxylate acid and carbon dioxide. During this route, harmful metabolites can be formed. Some of these intermediates could be more harmful than the initial pollutant, such as 1,4-benzoquinone, benzoic acid and benzaldehyde.[107,108] In order to understand the degradation pathways, the global toxicity of the solution was studied. ACT itself shows a low inhibition percentage (8%) as it is not a hazardous pollutant for this strain of bacteria (Fig. 11e and f). After 15 min time contact between the solution and *V. fischeri* bacteria, the acute toxicity of the treated solution strain increased rapidly at the early stage of the treatment and reached 72% after 2 h visible irradiation (Fig. 11e) and 68% at 15 min UV irradiation (Fig. 11f). This result is relevant and consistent with regard to the previously proven formation of toxic aromatic by-products such as 1,4-benzoquinone, benzoic acid and benzaldehyde.[74–76] After 3 h UV irradiation and 12 h degradation under visible light, the toxicity markedly declined to a value near 0% inhibition and lower than the initial % of inhibition of ACT. At that point, short-chain carboxylic acids and aromatic compounds could be formed continuously and then transformed to non-toxic compounds. Further studies should be done to identify all the byproducts of this degradation mechanism. As mentioned before, the photocatalyst used in this work has not been reported before, but a comparison with other works is summarized in Table 3. The comparison is not easy since many factors could vary such as pollutant concentration, catalyst concentration, pH of the solution and, most importantly, the irradiation type. However, it can be clearly seen that the prepared catalyst (TiO_2–BN–Pd) showed interesting results with a high degradation efficiency, recyclability and, most importantly, fast degradation rate.

4. Conclusion

To sum up, by combining two different techniques, electrospinning and ALD, six photocatalysts based on TiO_2 nanofibers coated by BN and Pd by ALD were synthesized: pristine TiO_2, TiO_2–Pd100, TiO_2–BN5, TiO_2–BN100, TiO_2–BN5–Pd100 and TiO_2–BN100–Pd100. The influence of the nanocomposite catalyst on the degradation of water pollutants was studied, using ACT as a model pollutant. XRD and Raman spectroscopy results indicate that the modification mechanism by ALD allowed the combination of crystalline phases of TiO_2 with different percentages of anatase–rutile phase. Moreover, TEM images showed the good dispersion of Pd NPs on the surface of the nanofibers, and the amount of Pd decreased with the increase of BN cycles. TiO_2/BN/Pd samples showed the best photocatalytic activity regarding ACT visible light irradiation (9 times higher than bare TiO_2), though their efficiency depends on the Schottky barrier-type separation from the deposition of another heterojunction material and noble metals on TiO_2. PL and EIS results confirmed that TiO_2–BN–Pd hybrids possess a superior charge separation ability from TiO_2, TiO_2–BN and TiO_2–Pd, which was devoted to higher degradation efficiency. Finally, the use of the ALD technique to modify the interface of TiO_2 shows a very promising pathway to enhance the degradation of micropollutants and their intermediates in wastewater, by allowing a conformal coating with thickness control and formation of composite materials. Although additional studies should be conducted with other pollutants and on wastewater to estimate the real efficiency of the prepared nanomaterials, the results presented open prospects for the tuning of photocatalysts by ALD.

Conflicts of interest

There are no conflicts to declare.

Acknowledgements

This study was financially supported by the French National Agency (ANR, program MeNiNA-ANR-17-CE09-0049). The authors thank Bruno Navarra (CNRS-IEM) for his technical assistance on ALD. The authors would also like to acknowledge Valérie Flaud (ICGM, France) for XPS technical support. I. I. acknowledges the partial financial support from the National Science Centre (NCN) of Poland by the SONATA-BIS grant 2020/38/E/ST5/00176.

References

1 M. M. Mekonnen and A. Y. Hoekstra, Four billion people facing severe water scarcity, *Sci. Adv.*, 2016, **2**(2), e1500323.

2 K. P. Gopinath, N. V. Madhav, A. Krishnan, R. Malolan and G. Rangarajan, Present applications of titanium dioxide for the photocatalytic removal of pollutants from water: A review, *J. Environ. Manage.*, 2020, **270**, 110906, DOI: 10.1016/j.jenvman.2020.110906.

3 C. Hou, T. Jiao, R. Xing, Y. Chen, J. Zhou and L. Zhang, Preparation of TiO2 nanoparticles modified electrospun nanocomposite membranes toward efficient dye degradation for wastewater treatment, *J. Taiwan Inst. Chem. Eng.*, 2017, **78**, 118–126, DOI: 10.1016/j.jtice.2017.04.033.

4 B. Singh, G. Kaur, P. Singh, *et al.*, Nanostructured BN–TiO2 composite with ultra-high photocatalytic activity, *New J. Chem.*, 2017, **41**(20), 11640–11646, DOI: 10.1039/C7NJ02509B.

5 X. Van Doorslaer, J. Dewulf, J. De Maerschalk, H. Van Langenhove and K. Demeestere, Heterogeneous photocatalysis of moxifloxacin in hospital effluent: Effect of selected matrix constituents, *Chem. Eng. J.*, 2015, **261**, 9–16, DOI: 10.1016/j.cej.2014.06.079.

6 A. A. Nada, B. O. Orimolade, H. H. El-Maghrabi, *et al.*, Photoelectrocatalysis of paracetamol on Pd–ZnO/N-doped carbon nanofibers electrode, *Appl. Mater. Today.*, 2021, **24**, 101129.

7 F. E. Titchou, H. Zazou, H. Afanga, *et al.*, Electrochemical oxidation treatment of Direct Red 23 aqueous solutions: Influence of the operating conditions, *Sep. Sci. Technol.*, 2021, **0**, 1–20, DOI: 10.1080/01496395.2021.1982978.

8 J. Zhang, X. Hou, Z. Pang, *et al.*, Fabrication of hierarchical TiO2 nanofibers by microemulsion electrospinning for photocatalysis applications, *Ceram. Int.*, 2017, **43**(17), 15911–15917, DOI: 10.1016/j.ceramint.2017.08.166. Published online.

9 M. Stucchi, C. L. Bianchi, C. Argirusis, *et al.*, Ultrasound assisted synthesis of Ag-decorated TiO2 active in visible light, *Ultrason. Sonochem.*, 2018, **40**, 282–288, DOI: 10.1016/j.ultsonch.2017.07.016.

10 M. Nasr, R. Viter, C. Eid, R. Habchi, P. Miele and M. Bechelany, Enhanced photocatalytic performance of novel electrospun BN/TiO2 composite nanofibers, *New J. Chem.*, 2017, **41**(1), 81–89, DOI: 10.1039/C6NJ03088B.

11 Q. Li, X. Hou, Z. Fang, *et al.*, Construction of layered h-BN/TiO2 hetero-structure and probing of the synergetic photocatalytic effect, *Sci. China Mater.*, 2020, **63**(2), 276–287, DOI: 10.1007/s40843-019-1180-8.

12 D. S. García-Zaleta, A. M. Torres-Huerta, M. A. Domínguez-Crespo, A. García-Murillo, R. Silva-Rodrigo and R. L. González, Influence of Phases Content on Pt/TiO2, Pd/TiO2 Catalysts for Degradation of 4-Chlorophenol at Room Temperature, *J. Nanomater.*, 2016, **2016**, 1805169, DOI: 10.1155/2016/1805169.

13 M. Wang, Z. Liu, M. Fang, *et al.*, Enhancement in the photocatalytic activity of TiO2 nano fibers hybridized with g-C3N4 via electrospinning, *Solid State Sci.*, 2016, **55**, 1–7, DOI: 10.1016/j.solidstatesciences.2016.02.002.

14 C. Zhou, C. Lai, C. Zhang, *et al.*, Semiconductor/boron nitride composites: Synthesis, properties, and photocatalysis applications, *Appl Catal., B*, 2018, **238**, 6–18, DOI: 10.1016/j.apcatb.2018.07.011.

15 S. Ramanavicius and A. Ramanavicius, Insights in the Application of Stoichiometric and Non-Stoichiometric Titanium Oxides for the Design of Sensors for the Determination of Gases and VOCs (TiO2−x and TinO2n−1 vs. TiO2), *Sensors*, 2020, **20**(23), 6833, DOI: 10.3390/s20236833.

16 S. Ramanavicius, A. Tereshchenko, R. Karpicz, *et al.*, TiO2-x/TiO2-structure based 'self-heated'sensor for the determination of some reducing gases, *Sensors*, 2020, **20**(1), 74.

17 M. Nasr, A. Abou Chaaya, N. Abboud, *et al.*, Photoluminescence: A very sensitive tool to detect the presence of anatase in rutile phase electrospun TiO2 nanofibers, *Superlattices Microstruct.*, 2015, **77**, 18–24, DOI: 10.1016/j.spmi.2014.10.034.

18 N. Sayed Farheen, O. D. Jayakumar, R. Sasikala, *et al.*, Photochemical Hydrogen Generation Using Nitrogen-Doped TiO2−Pd Nanoparticles: Facile Synthesis and

Effect of Ti3 + Incorporation, *J. Phys. Chem. C*, 2012, **116**(23), 12462–12467, DOI: 10.1021/jp3029962.
19 M. Nasr, S. Balme, C. Eid, R. Habchi, P. Miele and M. Bechelany, Enhanced Visible-Light Photocatalytic Performance of Electrospun rGO/TiO2 Composite Nanofibers, *J. Phys. Chem. C*, 2017, **121**(1), 261–269, DOI: 10.1021/acs.jpcc.6b08840.
20 H. Khan, Z. Jiang and D. Berk, Molybdenum doped graphene/TiO2 hybrid photocatalyst for UV/visible photocatalytic applications, *Sol. Energy*, 2018, **162**, 420–430, DOI: 10.1016/j.solener.2018.01.055.
21 P. Pascariu, A. Airinei, F. Iacomi, S. Bucur and M. P. Suchea, Chapter 12 - Electrospun TiO2-based nanofiber composites and their bio-related and environmental applications, in *Functional Nanostructured Interfaces for Environmental and Biomedical Applications*, ed. V. Dinca and M. P. Suchea, Elsevier; 2019, pp. 307–321. DOI: 10.1016/B978-0-12-814401-5.00012-8.
22 Z. Chen, J. Zhao, X. Yang, *et al.*, Fabrication of TiO2/WO3 Composite Nanofibers by Electrospinning and Photocatalystic Performance of the Resultant Fabrics, *Ind. Eng. Chem. Res.*, 2016, **55**(1), 80–85, DOI: 10.1021/acs.iecr.5b03578.
23 V. Shanmugam, S. Sanjeevamuthu, K. S. Jeyaperumal and R. Vairamuthu, Fabrication of heterostructured vanadium modified g-C3N4/TiO2 hybrid photocatalyst for improved photocatalytic performance under visible light exposure and antibacterial activities, *J. Ind. Eng. Chem.*, 2019, **76**, 318–332, DOI: 10.1016/j.jiec.2019.03.056.
24 L. Lin, H. Wang and P. Xu, Immobilized TiO2-reduced graphene oxide nanocomposites on optical fibers as high performance photocatalysts for degradation of pharmaceuticals, *Chem. Eng. J.*, 2017, **310**, 389–398, DOI: 10.1016/j.cej.2016.04.024.
25 W. Tao, M. Wang, R. Ali, *et al.*, Multi-layered porous hierarchical TiO2/g-C3N4 hybrid coating for enhanced visible light photocatalysis, *Appl. Surf. Sci.*, 2019, **495**, 143435, DOI: 10.1016/j.apsusc.2019.07.177.
26 A. Barhoum, H. H. El-Maghrabi, I. Iatsunskyi, *et al.*, Atomic layer deposition of Pd nanoparticles on self-supported carbon-Ni/NiO-Pd nanofiber electrodes for electrochemical hydrogen and oxygen evolution reactions, *J. Colloid Interface Sci.*, 2020, **569**, 286–297, DOI: 10.1016/j.jcis.2020.02.063.
27 H. Khojasteh, M. Salavati-niasari and F. Sadat, Photocatalytic evaluation of RGO/TiO 2 NWs/Pd-Ag nanocomposite as an improved catalyst for efficient dye degradation, *J. Alloys Compd.*, 2018, **746**, 611–618, DOI: 10.1016/j.jallcom.2018.02.345.
28 Y. Zhu, C. Gao, S. Bai, *et al.*, Hydriding Pd cocatalysts: An approach to giant enhancement on photocatalytic CO_2 reduction into CH4, *Nano Res.*, 2017, **10**, 1–11, DOI: 10.1007/s12274-017-1552-0.
29 H. Duan, Z. Wang, L. Cui, B. Lin and Y. Zhou, Stability Investigation of a Supported TiO2–Pd Bifunctional Catalyst over the One-Pot Liquid-Phase Synthesis of Methyl Isobutyl Ketone from Acetone and H2, *Ind. Eng. Chem. Res.*, 2018, **57**(37), 12358–12366, DOI: 10.1021/acs.iecr.8b02854.
30 M. R. Espino-Estévez, C. Fernández-Rodríguez, O. M. González-Díaz, *et al.*, Effect of TiO2–Pd and TiO2–Ag on the photocatalytic oxidation of diclofenac, isoproturon and phenol, *Chem. Eng. J.*, 2016, **298**, 82–95, DOI: 10.1016/j.cej.2016.04.016.
31 A. Meng, L. Zhang, B. Cheng and J. Yu, Dual Cocatalysts in TiO2 Photocatalysis, *Adv. Mater.*, 2019, **31**(30), 1807660, DOI: 10.1002/adma.201807660.
32 G. Jiang, K. Geng, Y. Wu, Y. Han and X. Shen, High photocatalytic performance of ruthenium complexes sensitizing g-C3N4/TiO2 hybrid in visible light irradiation, *Appl. Catal., B*, 2018, **227**, 366–375, DOI: 10.1016/j.apcatb.2018.01.034.
33 M. Nasr, L. Soussan, R. Viter, *et al.*, High photodegradation and antibacterial activity of BN–Ag/TiO2 composite nanofibers under visible light, *New J. Chem.*, 2018, **42**(2), 1250–1259, DOI: 10.1039/C7NJ03183A.
34 C. Lee, K. Na, W. Kim, D. Park, W. Yang and W. Choi, applied sciences TiO 2/ZnO Nanofibers Prepared by Electrospinning and Their Photocatalytic Degradation of Methylene Blue Compared with TiO 2 Nanofibers. Published online 2019.
35 S. M. Park, A. Razzaq, Y. H. Park, *et al.*, Hybrid CuxO–TiO2 Heterostructured Composites for Photocatalytic CO_2 Reduction into Methane Using Solar Irradiation: Sunlight into Fuel, *ACS Omega*, 2016, **1**(5), 868–875, DOI: 10.1021/acsomega.6b00164.
36 C. Peng, X. Yang, Y. Li, H. Yu, H. Wang and F. Peng, Hybrids of Two-Dimensional Ti3C2 and TiO2 Exposing {001} Facets toward Enhanced Photocatalytic Activity, *ACS Appl. Mater. Interfaces*, 2016, **8**(9), 6051–6060, DOI: 10.1021/acsami.5b11973.
37 E. Coy, K. Siuzdak, I. Grądzka-Kurzaj, *et al.*, Exploring the effect of BN and BN bridges on the photocatalytic performance of semiconductor heterojunctions: Enhancing carrier transfer mechanism, *Appl. Mater. Today*, 2021, **24**, 101095.
38 M. Bechelany, A. Brioude, P. Stadelmann, S. Bernard, D. Cornu and P. Miele, Preparation of BN Microtubes/Nanotubes with a Unique Chemical Process, *J. Phys. Chem. C*, 2008, **112**(47), 18325–18330, DOI: 10.1021/jp804286x.
39 X. Gao, Y. Yao and X. Meng, Recent development on BN-based photocatalysis: A review, *Mater. Sci. Semicond. Process*, 2020, **120**, 105256, DOI: 10.1016/j.mssp.2020.105256.
40 L. Lin, L. Lin, W. Jiang, M. Bechelany, M. Nasr and J. Jarvis, Adsorption and photocatalytic oxidation of ibuprofen using nanocomposites of TiO2 nanofibers combined with BN nanosheets : Degradation products and mechanisms Chemosphere Adsorption and photocatalytic oxidation of ibuprofen using nanocomposites of TiO 2 n, *Chemosphere*, 2019, **220**(December 2018), 921–929, DOI: 10.1016/j.chemosphere.2018.12.184.

41 Y. Sheng, J. Yang, F. Wang, *et al.*, Sol-gel synthesized hexagonal boron nitride/titania nanocomposites with enhanced photocatalytic activity, *Appl. Surf. Sci.*, 2019, **465**, 154–163, DOI: 10.1016/j.apsusc.2018.09.137.

42 Z. Li and X. Meng, Recent development on palladium enhanced photocatalytic activity: A review, *J. Alloys Compd.*, 2020, **830**, 154669, DOI: 10.1016/j.jallcom.2020.154669.

43 E. Coy, K. Siuzdak, M. Pavlenko, *et al.*, Enhancing photocatalytic performance and solar absorption by schottky nanodiodes heterojunctions in mechanically resilient palladium coated TiO2/Si nanopillars by atomic layer deposition, *Chem. Eng. J.*, 2020, **392**, 123702, DOI: 10.1016/j.cej.2019.123702.

44 S. Linic, U. Aslam, C. Boerigter and M. Morabito, Photochemical transformations on plasmonic metal nanoparticles, *Nat. Mater.*, 2015, **14**(6), 567–576, DOI: 10.1038/nmat4281.

45 S. K. Mohapatra, N. Kondamudi, S. Banerjee and M. Misra, Functionalization of Self-Organized TiO2 Nanotubes with Pd Nanoparticles for Photocatalytic Decomposition of Dyes under Solar Light Illumination, *Langmuir*, 2008, **24**(19), 11276–11281, DOI: 10.1021/la801253f.

46 Z. Wu, Z. Sheng, Y. Liu, H. Wang, N. Tang and J. Wang, Characterization and activity of Pd-modified TiO2 catalysts for photocatalytic oxidation of NO in gas phase, *J. Hazard. Mater.*, 2009, **164**(2), 542–548, DOI: 10.1016/j.jhazmat.2008.08.028.

47 B. Rusinque and H. Lasa, Photoreduction of a Pd-Doped Mesoporous TiO2 Photocatalyst for Hydrogen Production under Visible Light, *Catalysts*, 2020, **10**, 74, DOI: 10.3390/catal10010074.

48 R. Drunka, J. Grabis and A. Krūmiņa, Preparation of Au, Pt, Pd and Ag Doped TiO2 Nanofibers and their Photocatalytic Properties under LED Illumination, *Key Eng. Mater.*, 2018, **762**, 283–287, DOI: 10.4028/www.scientific.net/KEM.762.283.

49 Q. Tang, X. Meng, Z. Wang, J. Zhou and H. Tang, One-step Electrospinning Synthesis of TiO 2/g-C 3 N 4 Nanofibers with Enhanced Photocatalytic Properties, *Appl. Surf. Sci.*, 2018, **430**, 253–262, DOI: 10.1016/j.apsusc.2017.07.288.

50 M. Weber, A. Julbe, A. Ayral, P. Miele and M. Bechelany, Atomic Layer Deposition for Membranes: Basics, Challenges, and Opportunities, *Chem. Mater.*, 2018, **30**(21), 7368–7390, DOI: 10.1021/acs.chemmater.8b02687.

51 O. Graniel, M. Weber, S. Balme, P. Miele and M. Bechelany, Atomic layer deposition for biosensing applications, *Biosens. Bioelectron.*, 2018, **122**, 147–159, DOI: 10.1016/j.bios.2018.09.038.

52 A. J. M. Mackus, M. J. Weber, N. F. W. Thissen, *et al.*, Atomic layer deposition of Pd and Pt nanoparticles for catalysis: on the mechanisms of nanoparticle formation, *Nanotechnology*, 2015, **27**(3), 034001, DOI: 10.1088/0957-4484/27/3/034001.

53 M. Najem, A. A. Nada, M. Weber, *et al.*, Palladium/Carbon Nanofibers by Combining Atomic Layer Deposition and Electrospinning for Organic Pollutant Degradation, *Materials*, 2020, **13**(8), 1947, DOI: 10.3390/ma13081947.

54 M. Weber and M. Bechelany, Combining nanoparticles grown by ALD and MOFs for gas separation and catalysis applications, *Pure Appl. Chem.*, 2020, **92**(2), 213–222, DOI: 10.1515/pac-2019-0109.

55 R. K. Ramachandran, C. Detavernier and J. Dendooven, Atomic Layer Deposition for Catalysis, in *Nanotechnology in Catalysis*, John Wiley & Sons, Ltd, 2017, pp. 335–358. DOI: 10.1002/9783527699827.ch14.

56 S. M. George, Atomic Layer Deposition: An Overview, *Chem. Rev.*, 2010, **110**(1), 111–131, DOI: 10.1021/cr900056b.

57 M. Weber, M. Verheijen, A. Bol and W. Kessels, Sub-nanometer dimensions control of core/shell nanoparticles prepared by atomic layer deposition, *Nanotechnology*, 2015, **26**(9), 094002.

58 N. K. R. Eswar, S. A. Singh and J. Heo, Atomic layer deposited photocatalysts: comprehensive review on viable fabrication routes and reactor design approaches for photo-mediated redox reactions, *J. Mater. Chem. A*, 2019, **7**(30), 17703–17734, DOI: 10.1039/C9TA04780H.

59 M. Weber, N. Tuleushova, J. Zgheib, *et al.*, Enhanced electrocatalytic performance triggered by atomically bridged boron nitride between palladium nanoparticles and carbon fibers in gas-diffusion electrodes, *Appl. Catal., B*, 2019, **257**, 117917, DOI: 10.1016/j.apcatb.2019.117917.

60 S. Vempati, K. S. Ranjith, F. Topuz, N. Biyikli and T. Uyar, Electrospinning Combined with Atomic Layer Deposition to Generate Applied Nanomaterials: A Review, *ACS Appl. Nano Mater.*, 2020, **3**(7), 6186–6209, DOI: 10.1021/acsanm.0c01120.

61 A. Barhoum, K. Pal, H. Rahier, H. Uludag, I. S. Kim and M. Bechelany, Nanofibers as new-generation materials: From spinning and nano-spinning fabrication techniques to emerging applications, *Appl. Mater. Today*, 2019, **17**, 1–35, DOI: 10.1016/j.apmt.2019.06.015.

62 S. M. Pasini, A. Valério, G. Yin, *et al.*, An overview on nanostructured TiO2–containing fibers for photocatalytic degradation of organic pollutants in wastewater treatment, *J. Water Process Eng.*, 2021, **40**, 101827, DOI: 10.1016/j.jwpe.2020.101827.

63 S. Mozzaquatro, A. Valério, S. M. A. Guelli, *et al.*, Journal of Environmental Chemical Engineering Plasma-modi fi ed TiO 2/polyetherimide nanocomposite fi bers for photocatalytic degradation of organic compounds, *J. Environ. Chem. Eng.*, 2019, **7**(4), 103213, DOI: 10.1016/j.jece.2019.103213.

64 Q. Tang, X. Meng, Z. Wang, J. Zhou and H. Tang, One-step electrospinning synthesis of TiO2/g-C3N4 nanofibers with enhanced photocatalytic properties, *Appl. Surf. Sci.*, 2018, **430**, 253–262, DOI: 10.1016/j.apsusc.2017.07.288.

65 P. S. Basavarajappa, S. B. Patil, N. Ganganagappa, K. R. Reddy, A. V. Raghu and C. Reddy, Recent progress in metal-doped TiO2, non-metal doped/codoped TiO2 and TiO2 nanostructured hybrids for enhanced photocatalysis,

Int. J. Hydrogen Energy, 2020, **45**(13), 7764–7778, DOI: 10.1016/j.ijhydene.2019.07.241.

66 T. P. Shende, B. A. Bhanvase, A. P. Rathod, D. V. Pinjari and S. H. Sonawane, Sonochemical synthesis of Graphene-Ce-TiO2 and Graphene-Fe-TiO2 ternary hybrid photocatalyst nanocomposite and its application in degradation of crystal violet dye, *Ultrason. Sonochem.*, 2018, **41**, 582–589, DOI: 10.1016/j.ultsonch.2017.10.024.

67 A. Meng, L. Zhang, B. Cheng and J. Yu, TiO2–MnOx–Pt Hybrid Multiheterojunction Film Photocatalyst with Enhanced Photocatalytic CO_2-Reduction Activity, *ACS Appl. Mater. Interfaces*, 2019, **11**(6), 5581–5589, DOI: 10.1021/acsami.8b02552.

68 M. Nasr, C. Eid, R. Habchi and P. Miele, Recent Progress on Titanium Dioxide Nanomaterials for Photocatalytic Applications, *ChemSusChem.*, 2018, **11**(18), 3023–3047, DOI: 10.1002/cssc.201800874.

69 I. S. Chronakis, Novel nanocomposites and nanoceramics based on polymer nanofibers using electrospinning process—A review, *J. Mater. Process. Technol.*, 2005, **167**(2), 283–293, DOI: 10.1016/j.jmatprotec.2005.06.053.

70 D. H. Reneker and A. L. Yarin, Electrospinning jets and polymer nanofibers, *Polymer.*, 2008, **49**(10), 2387–2425, DOI: 10.1016/j.polymer.2008.02.002.

71 A. Merenda, M. Weber, M. Bechelany, *et al.*, Fabrication of Pd-TiO2 nanotube photoactive junctions via Atomic Layer Deposition for persistent pesticide pollutants degradation, *Appl. Surf. Sci.*, 2019, **483**, 219–230, DOI: 10.1016/j.apsusc.2019.03.285.

72 M. Weber, M. Drobek, B. Rebière, *et al.*, Hydrogen selective palladium-alumina composite membranes prepared by Atomic Layer Deposition, *J. Membr. Sci.*, 2020, **596**, 117701, DOI: 10.1016/j.memsci.2019.117701.

73 M. Weber, J. H. Kim, J. H. Lee, *et al.*, High-Performance Nanowire Hydrogen Sensors by Exploiting the Synergistic Effect of Pd Nanoparticles and Metal–Organic Framework Membranes, *ACS Appl. Mater. Interfaces*, 2018, **10**(40), 34765–34773, DOI: 10.1021/acsami.8b12569.

74 R. Molenaar, J. Jaap and J. R. Zijp, Determination of Kubelka–Munk scattering and absorption coefficients by diffuse illumination, *Appl. Opt.*, 1999, **38**(10), 2068–2077.

75 I. K. Konstantinou and T. A. Albanis, TiO2-assisted photocatalytic degradation of azo dyes in aqueous solution: kinetic and mechanistic investigations: A review, *Appl. Catal., B*, 2004, **49**(1), 1–14, DOI: 10.1016/j.apcatb.2003.11.010.

76 I. K. Konstantinou and T. A. Albanis, Photocatalytic transformation of pesticides in aqueous titanium dioxide suspensions using artificial and solar light: intermediates and degradation pathways, *Appl. Catal., B*, 2003, **42**(4), 319–335, DOI: 10.1016/S0926-3373(02)00266-7.

77 T. Xuan, H. Le, N. T. Van, *et al.*, Correlation between degradation pathway and toxicity of acetaminophen and its by-products by using the electro-Fenton process in aqueous media, *Chemosphere*, 2017, **172**, 1–9, DOI: 10.1016/j.chemosphere.2016.12.060.

78 M. El Kateb, C. Trellu, A. Darwich, *et al.*, Electrochemical advanced oxidation processes using novel electrode materials for mineralization and biodegradability enhancement of nanofiltration concentrate of landfill leachates, *Water Res.*, 2019, **162**, 446–455.

79 R. A. Spurr and H. Myers, Quantitative analysis of anatase-rutile mixtures with an X-ray diffractometer, *Anal. Chem.*, 1957, **29**(5), 760–762.

80 Q. Xu, *Nanoporous Materials: Synthesis and Applications*, CRC press, 2013.

81 H. Li, W. Zhang and W. Pan, Enhanced Photocatalytic Activity of Electrospun TiO2 Nanofibers with Optimal Anatase/Rutile Ratio, *J. Am. Ceram. Soc.*, 2011, **94**(10), 3184–3187, DOI: 10.1111/j.1551-2916.2011.04748.x.

82 X. Fan, T. Yu, L. Zhang, X. Chen and Z. Zou, Photocatalytic degradation of acetaldehyde on mesoporous TiO2: Effects of surface area and crystallinity on the photocatalytic activity, *Chin. J. Chem. Phys.*, 2007, **20**(6), 733.

83 C. Zhang, Y. Li, Y. Wang and H. He, Sodium-Promoted Pd/TiO2 for Catalytic Oxidation of Formaldehyde at Ambient Temperature, *Environ. Sci. Technol.*, 2014, **48**(10), 5816–5822, DOI: 10.1021/es4056627.

84 W. Ouyang, S. Liu, K. Yao, *et al.*, Ultrafine hollow TiO2 nanofibers from core-shell composite fibers and their photocatalytic properties, *Compos. Commun.*, 2018, **9**, 76–80, DOI: 10.1016/j.coco.2018.06.006.

85 S. Kawrani, A. A. Nada, M. F. Bekheet, *et al.*, Enhancement of calcium copper titanium oxide photoelectrochemical performance using boron nitride nanosheets, *Chem. Eng. J.*, 2020, **389**, 124326, DOI: 10.1016/j.cej.2020.124326.

86 A. A. Nada, W. M. A. El Rouby, M. F. Bekheet, *et al.*, Highly textured boron/nitrogen co-doped TiO2 with honeycomb structure showing enhanced visible-light photoelectrocatalytic activity, *Appl. Surf. Sci.*, 2020, **505**, 144419, DOI: 10.1016/j.apsusc.2019.144419.

87 A. S. Bolokang, D. E. Motaung, C. J. Arendse and T. F. G. Muller, Morphology and structural development of reduced anatase-TiO2 by pure Ti powder upon annealing and nitridation: Synthesis of TiOx and TiOxNy powders, *Mater. Charact.*, 2015, **100**, 41–49, DOI: 10.1016/j.matchar.2014.11.026.

88 M. Zhang, D. Lu, G. Yan, J. Wu and J. Yang, Fabrication of Mo + N-Codoped TiO2 Nanotube Arrays by Anodization and Sputtering for Visible Light-Induced Photoelectrochemical and Photocatalytic Properties, in *J Nanomater*, ed. S. Zhu, 2013, vol. 2013, p. 648346. DOI: 10.1155/2013/648346.

89 C. Byrne, R. Fagan, S. Hinder, D. E. McCormack and S. C. Pillai, New approach of modifying the anatase to rutile transition temperature in TiO2 photocatalysts, *RSC Adv.*, 2016, **6**(97), 95232–95238, DOI: 10.1039/C6RA19759K.

90 P. Yilmaz, A. M. Lacerda, I. Larrosa and S. Dunn, Photoelectrocatalysis of Rhodamine B and Solar Hydrogen Production by TiO2 and Pd/TiO2 Catalyst Systems,

Electrochim. Acta, 2017, **231**, 641–649, DOI: 10.1016/j.electacta.2017.02.035.

91 C. H. Nguyen, C. C. Fu and R. S. Juang, Degradation of methylene blue and methyl orange by palladium-doped TiO2 photocatalysis for water reuse: Efficiency and degradation pathways, *J. Cleaner Prod.*, 2018, **202**, 413–427, DOI: 10.1016/j.jclepro.2018.08.110.

92 I. Iatsunskyi, M. Pavlenko, R. Viter, *et al.*, Tailoring the Structural, Optical, and Photoluminescence Properties of Porous Silicon/TiO2 Nanostructures, *J. Phys. Chem. C*, 2015, **119**(13), 7164–7171, DOI: 10.1021/acs.jpcc.5b01670.

93 H. Safajou, H. Khojasteh, M. Salavati-Niasari and S. Mortazavi-Derazkola, Enhanced photocatalytic degradation of dyes over graphene/Pd/TiO2 nanocomposites: TiO2 nanowires versus TiO2 nanoparticles, *J. Colloid Interface Sci.*, 2017, **498**, 423–432, DOI: 10.1016/j.jcis.2017.03.078.

94 I. Levchuk, C. Guillard, F. Dappozze, S. Parola, D. Leonard and M. Sillanpää, Photocatalytic activity of TiO2 films immobilized on aluminum foam by atomic layer deposition technique, *J. Photochem. Photobiol., A*, 2016, **328**, 16–23, DOI: 10.1016/j.jphotochem.2016.03.034.

95 N. Serpone, Relative photonic efficiencies and quantum yields in heterogeneous photocatalysis, *J. Photochem. Photobiol., A.*, 1997, **104**(1), 1–12, DOI: 10.1016/S1010-6030(96)04538-8.

96 D. García-Zaleta, J. Montes de Oca-Valero and A. M. Torres-Huerta, *et al.*, *Effect of Pd addition on the nanostructure and properties of Pd/TiO2 catalysts for the photocatalytic degradation of 4-chlorophenol*, Trans Tech Publ, 2014, vol 28, pp. 9–20.

97 Y. Ide, F. Liu, J. Zhang, *et al.*, Hybridization of Au nanoparticle-loaded TiO2 with BN nanosheets for efficient solar-driven photocatalysis, *J. Mater. Chem. A*, 2014, **2**(12), 4150–4156, DOI: 10.1039/C3TA13769D.

98 S. Zhu and D. Wang, Photocatalysis: Basic Principles, Diverse Forms of Implementations and Emerging Scientific Opportunities, *Adv. Energy Mater.*, 2017, **7**(23), 1700841, DOI: 10.1002/aenm.201700841.

99 J. Singh, N. Tripathi and S. Mohapatra, Synthesis of Ag–TiO2 hybrid nanoparticles with enhanced photocatalytic activity by a facile wet chemical method, *Nano-Struct. Nano-Objects*, 2019, **18**, 100266, DOI: 10.1016/j.nanoso.2019.100266.

100 H. Khan, M. G. Rigamonti and D. C. Boffito, Enhanced photocatalytic activity of Pt-TiO2/WO3 hybrid material with energy storage ability, *Appl. Catal., B*, 2019, **252**, 77–85, DOI: 10.1016/j.apcatb.2019.04.019.

101 K. H. Leong, H. Y. Chu, S. Ibrahim and P. Saravanan, Palladium nanoparticles anchored to anatase TiO2 for enhanced surface plasmon resonance-stimulated, visible-light-driven photocatalytic activity, *Beilstein J. Nanotechnol.*, 2015, **6**(1), 428–437.

102 C. C. Chan, C. C. Chang, W. C. Hsu, S. K. Wang and J. Lin, Photocatalytic activities of Pd-loaded mesoporous TiO2 thin films, *Chem. Eng. J.*, 2009, **152**(2), 492–497, DOI: 10.1016/j.cej.2009.05.012.

103 A. A. Nada, M. F. Bekheet, R. Viter, P. Miele, S. Roualdes and M. Bechelany, BN/GdxTi (1-x) O (4-x)/2 nanofibers for enhanced photocatalytic hydrogen production under visible light, *Appl. Catal., B*, 2019, **251**, 76–86.

104 R. Elshypany, H. Selim, K. Zakaria, *et al.*, Elaboration of Fe3O4/ZnO nanocomposite with highly performance photocatalytic activity for degradation methylene blue under visible light irradiation, *Environ. Technol. Innovation*, 2021, **23**, 101710, DOI: 10.1016/j.eti.2021.101710.

105 L. Lin, W. Jiang, M. Nasr, *et al.*, Enhanced visible light photocatalysis by TiO 2–BN enabled electrospinning of nanofibers for pharmaceutical degradation and wastewater treatment, *Photochem. Photobiol. Sci.*, 2019, **18**(12), 2921–2930.

106 X. Zhang, F. Wu, X. Wu, P. Chen and N. Deng, Photodegradation of acetaminophen in TiO2 suspended solution, *J. Hazard. Mater.*, 2008, **157**(2), 300–307, DOI: 10.1016/j.jhazmat.2007.12.098.

107 M. D. G. de Luna, M. L. Veciana, C. C. Su and M. C. Lu, Acetaminophen degradation by electro-Fenton and photoelectro-Fenton using a double cathode electrochemical cell, *J. Hazard. Mater.*, 2012, **217–218**, 200–207, DOI: 10.1016/j.jhazmat.2012.03.018.

108 H. N. P. Vo, G. K. Le, T. M. H. Nguyen, *et al.*, Acetaminophen micropollutant: Historical and current occurrences, toxicity, removal strategies and transformation pathways in different environments, *Chemosphere*, 2019, **236**, 124391, DOI: 10.1016/j.chemosphere.2019.124391.

109 O. Nasr, O. Mohamed, A. S. Al-Shirbini and A. M. Abdel-Wahab, Photocatalytic degradation of acetaminophen over Ag, Au and Pt loaded TiO2 using solar light, *J. Photochem. Photobiol., A.*, 2019, **374**, 185–193, DOI: 10.1016/j.jphotochem.2019.01.032.

110 C. A. Aguilar, C. Montalvo, J. G. Ceron and E. Moctezuma, Photocatalytic Degradation of Acetaminophen, *Int. J. Environ. Res.*, 2011, **5**(4), 1071–1078, DOI: 10.22059/ijer.2011.465.

111 C. A. Aguilar, C. Montalvo, B. B. Zermeño, *et al.*, Photocatalytic degradation of acetaminophen, tergitol and nonylphenol with catalysts TiO2/Ag under UV and Vis light, *Int. J. Environ. Sci. Technol.*, 2019, **16**(2), 843–852, DOI: 10.1007/s13762-018-1707-x.

112 J. C. T. Lin, M. D. G. de Luna, G. L. Aranzamendez and M. C. Lu, Degradations of acetaminophen via a K2S2O8-doped TiO2 photocatalyst under visible light irradiation, *Chemosphere*, 2016, **155**, 388–394, DOI: 10.1016/j.chemosphere.2016.04.059.

113 G. Ni, Y. Li, S. Wang and Q. Li, Construction of 1D/2D BN/TiO2 nanostructures for efficient photocatalytic degradation of dyes, *Mater. Lett.*, 2021, **288**, 129385, DOI: 10.1016/j.matlet.2021.129385.

114 B. Czech and K. Tyszczuk-Rotko, Visible-light-driven photocatalytic removal of acetaminophen from water using a novel MWCNT-TiO2-SiO2 photocatalysts, *Sep. Purif. Technol.*, 2018, **206**, 343–355, DOI: 10.1016/j.seppur.2018.06.025.

115 O. F. S. Khasawneh, P. Palaniandy, M. Ahmadipour and H. Mohammadi, Bin Hamdan MR. Removal of acetaminophen using Fe2O3-TiO2 nanocomposites by photocatalysis under simulated solar irradiation: Optimization study, *J. Environ. Chem. Eng.*, 2021, **9**(1), 104921, DOI: 10.1016/j.jece.2020.104921.

116 T. A. Kurniawan, L. Yanyan, T. Ouyang, A. B. Albadarin and G. Walker, BaTiO3/TiO2 composite-assisted photocatalytic degradation for removal of acetaminophen from synthetic wastewater under UV–vis irradiation, *Mater. Sci. Semicond. Process.*, 2018, **73**, 42–50, DOI: 10.1016/j.mssp.2017.06.048.

117 A. H. Cheshme Khavar, G. Moussavi and A. R. Mahjoub, The preparation of TiO2@rGO nanocomposite efficiently activated with UVA/LED and H_2O_2 for high rate oxidation of acetaminophen: Catalyst characterization and acetaminophen degradation and mineralization, *Appl. Surf. Sci.*, 2018, **440**, 963–973, DOI: 10.1016/j.apsusc.2018.01.238.

118 L. Yanyan, T. A. Kurniawan, Z. Ying, A. B. Albadarin and G. Walker, Enhanced photocatalytic degradation of acetaminophen from wastewater using WO3/TiO2/SiO2 composite under UV–VIS irradiation, *J. Mol. Liq.*, 2017, **243**, 761–770, DOI: 10.1016/j.molliq.2017.08.092.

119 S. Ramasundaram, H. N. Yoo, K. G. Song, J. Lee, K. J. Choi and S. W. Hong, Titanium dioxide nanofibers integrated stainless steel filter for photocatalytic degradation of pharmaceutical compounds, *J. Hazard. Mater.*, 2013, **258–259**, 124–132, DOI: 10.1016/j.jhazmat.2013.04.047.